Article

Realization of a doped quantum antiferromagnet in a Rydberg tweezer array

https://doi.org/10.1038/s41586-025-09377-1

Received: 15 January 2025

Accepted: 9 July 2025

Published online: 20 August 2025

Check for updates

Mu Qiao[1,11]✉, Gabriel Emperauger[1,11], Cheng Chen[1,2,11], Lukas Homeier[3,4,11], Simon Hollerith[5,11], Guillaume Bornet[1], Romain Martin[1], Bastien Gély[1], Lukas Klein[1], Daniel Barredo[1,6], Sebastian Geier[7], Neng-Chun Chiu[5], Fabian Grusdt[8,9], Annabelle Bohrdt[9,10], Thierry Lahaye[1] & Antoine Browaeys[1]✉

Doping an antiferromagnetic (AFM) Mott insulator is central to our understanding of a variety of phenomena in strongly correlated electrons, including high-temperature superconductors[1,2]. To describe the competition between tunnelling t of hole dopants and AFM spin interactions J, theoretical and numerical studies often focus on the paradigmatic t–J model[3] and the direct analogue quantum simulation of this model in the relevant regime of high-particle density has long been sought[4,5]. Here we realize a doped quantum antiferromagnet with next-nearest-neighbour (NNN) tunnellings t' (refs. 6–10) and hard-core bosonic holes[11] using a Rydberg tweezer platform. We use coherent dynamics between three Rydberg levels, encoding spins and holes[12], to implement a tunable bosonic t–J–V model allowing us to study previously inaccessible parameter regimes. We observe dynamical phase separation between hole and spin domains for $|t/J| \ll 1$ and demonstrate the formation of repulsively bound hole pairs in a variety of spin backgrounds. The interference between NNN tunnellings t' and perturbative pair tunnelling gives rise to light and heavy pairs depending on the sign of t. Using the single-site control allows us to study the dynamics of a single hole in 2D square lattice (anti)ferromagnets. The model we implement extends the toolbox of Rydberg tweezer experiments beyond spin-1/2 models[13] to a larger class of t–J and spin-1 models[14,15].

The low-energy and out-of-equilibrium properties of materials with strong electronic interactions are notoriously difficult to model, both theoretically and numerically[16,17]. Although cuprate superconductors have been discovered almost four decades ago, a full understanding of the mechanisms underlying unconventional, high-temperature superconductivity is lacking[18,19]. The most intricate regime in the paradigmatic Fermi–Hubbard or t–J model[3] arises on doping the AFM Mott insulator[1], in which the kinetic motion t of holes competes with the magnetic ordering of spins. Understanding this interplay between magnetism and charge dynamics at low doping is important to develop phenomenological models of high-temperature superconductivity.

The controlled quantum simulation of many-body systems[20] has gained notable importance in the investigation of strongly correlated materials, and ubiquitous phenomena, such as long-range antiferromagnetism in the square[21] and cubic lattice[22], pairing in 1D ladders[23] or Nagaoka ferromagnetism in the triangular lattice[24,25], have been observed, among others[2]. So far, the leading platform for the quantum simulation of doped quantum magnets has been ultracold fermionic atoms in optical lattices[26,27]. In this system, the AFM spin coupling $J = 4t^2/U$ originates perturbatively from strong repulsive Hubbard interactions $U \gg t$, thereby restricting the parameter space to $t \gg J$ in the effective t–J model.

Although this is the most relevant regime for strongly correlated electrons, it prevents examination of many of the other theoretically predicted phases such as phase separation[28,29] or models with bosonic hole dopants[29–31], in which recent numerical studies have predicted stripe-ordered[12,32] and paired phases[33] suggesting a common mechanism underlying AFM t–J models. Recently, the preparation of negative temperature states in a Bose–Hubbard model studied the dynamics of a single hole in a bosonic antiferromagnet[11]. Notably, another promising route to directly realize t–J–V–W models with dipolar AFM interactions, that is, including more general hole–hole (spin–hole) interactions V (W), has recently been achieved in itinerant, fermionic polar molecules in optical lattices[4,5] enabling access to a greater parameter space. The implementation of tunnellings t beyond nearest-neighbour (NN) sites in optical lattices remains challenging but is desired to test predictions, such as their importance for superconductivity, which has received much attention recently[6–10]. To our knowledge, no direct realization of the t–J model has been achieved in the high particle filling regime with

[1]Université Paris-Saclay, Institut d'Optique Graduate School, CNRS, Laboratoire Charles Fabry, Palaiseau Cedex, France. [2]Institute of Physics, Chinese Academy of Sciences, Beijing, China. [3]JILA and Department of Physics, University of Colorado, Boulder, CO, USA. [4]Center for Theory of Quantum Matter, University of Colorado, Boulder, CO, USA. [5]Department of Physics, Harvard University, Cambridge, MA, USA. [6]Nanomaterials and Nanotechnology Research Center (CINN-CSIC), Universidad de Oviedo (UO), Principado de Asturias, El Entrego, Spain. [7]Physikalisches Institut, Universität Heidelberg, Heidelberg, Germany. [8]Department of Physics and Arnold Sommerfeld Center for Theoretical Physics (ASC), Ludwig-Maximilians-Universität München, München, Germany. [9]Munich Center for Quantum Science and Technology (MCQST), München, Germany. [10]University of Regensburg, Regensburg, Germany. [11]These authors contributed equally: Mu Qiao, Gabriel Emperauger, Cheng Chen, Lukas Homeier, Simon Hollerith. ✉e-mail: mu.q.phys@gmail.com; antoine.browaeys@institutoptique.fr

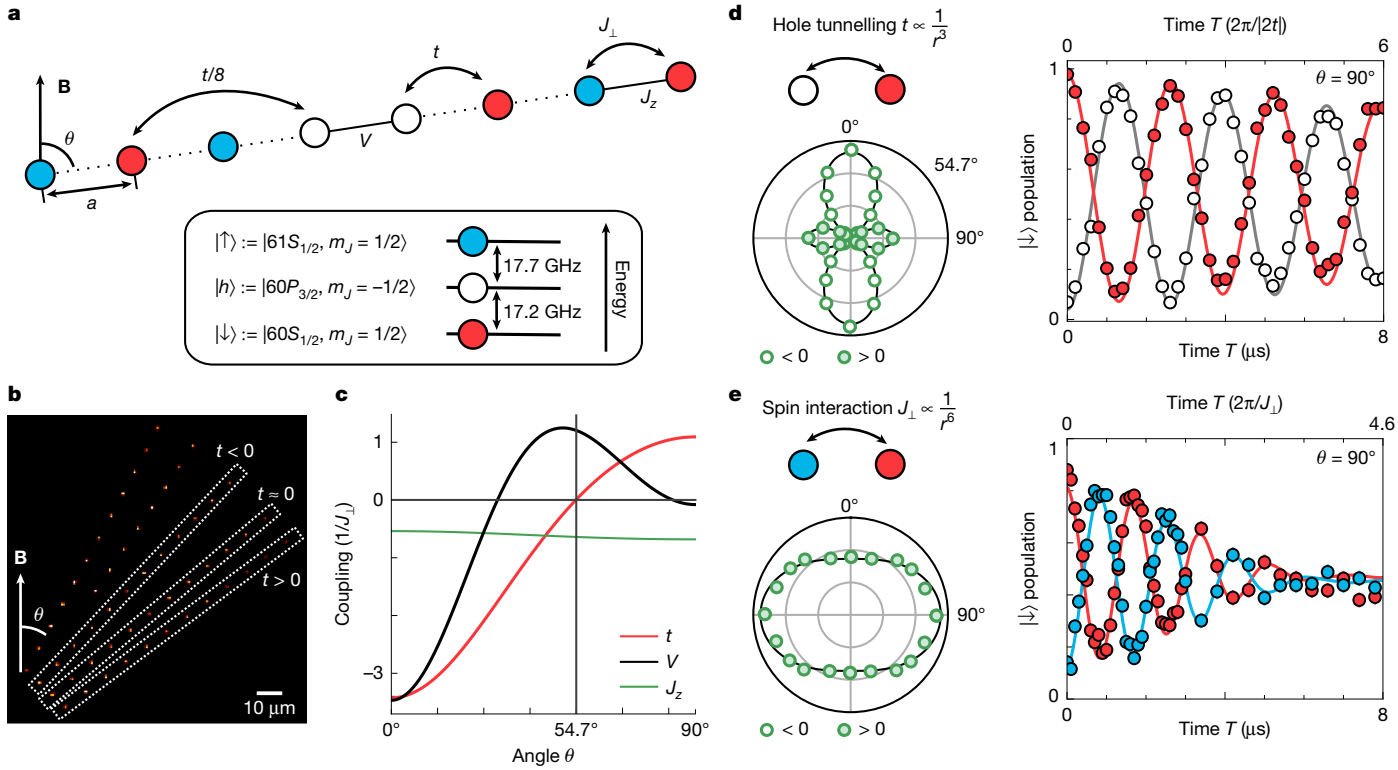

Fig. 1 | Implementation of the *t*–*J*–*V* model in a Rydberg tweezer array. **a**, The three Rydberg states $|61S_{1/2}\rangle$, $|60S_{1/2}\rangle$ and $|60P_{3/2}\rangle$ encode spin up ($|\uparrow\rangle$), spin down ($|\downarrow\rangle$) and hole ($|h\rangle$), respectively. The atomic pair interactions give rise to tunnellings ($t \propto r^{-3}$) and spin–spin ($J_\perp$,J_z) and hole–hole (V) interactions. **b**, Fluorescence image of 1D atomic arrays oriented at different angles θ relative to the quantization axis defined by the magnetic field **B**. For an experiment corresponding to a given θ, only the relevant chain is filled with atoms. Scale bar, 10 µm. **c**, Calculated angular dependence of the interaction strengths normalized to $J_\perp$, showing the tunability of the different terms in the *t*–*J*–*V* Hamiltonian at distance a = 9.9 µm. **d**,**e**, Measured angular dependence of interaction strength and coherent evolution using isolated atom pairs. The hole tunnelling t (**d**) exhibits strong angular variation with vanishing amplitude at the magic angle $\theta_m = 54.7°$, whereas the spin–spin interaction $J_\perp$ (**e**) shows weaker angular modulation. Filled (empty) green circles in the left panels indicate positive (negative) interaction amplitudes and black lines represent theoretically calculated interaction values. Right panels show the $|\downarrow\rangle$ population of two atoms undergoing coherent state exchange; the colour indicates the initial state of each atom. Solid lines show numerical simulations including thermal atomic motion[39].

single-site resolution nor has tunnelling beyond nearest neighbours been implemented.

As recently proposed in ref. 12, we encode the hole and spins into three Rydberg states of ^{87}Rb atoms. The dipole–dipole and the van der Waals interactions between atoms implement a hard-core bosonic *t*–*J*–*V* model, with at most one particle per site. The $1/r^3$ dipole–dipole interactions yield hole tunnelling $\propto t$ and the $1/r^6$ van der Waals interactions realize magnetic spin coupling $\propto J_\perp, J_z$ and hole–hole interactions $\propto V$. In a 1D chain, the tweezers set-up allows us to tune the ratio between hole tunnelling t, spin interaction $J_{\perp,z}$ and hole–hole interaction V over a large range by changing the orientation of the chain with respect to the quantization axis. In a 2D array, the ratio t/J can be tuned by varying the site distance. In both cases, we can access the regimes $t \ll J_\perp$ and $t \gg J_\perp$. In our implementation, we study the dynamical properties of doped 1D and 2D quantum magnets with long-range dipolar tunnelling.

In this model, the interplay between tunnelling t and AFM spin flip-flop interactions $J_\perp$ introduces a 'sign problem', even when the exchange statistics of holes is bosonic[33]. At high particle density, this frustration leads to strong spin–charge correlations[12], such as paired phases[33]. Although the statistics plays a crucial role for collective properties, our model explores underlying mechanisms, including magnetically mediated pairing mechanisms[34,35] or kinetic magnetism[36]. Furthermore, the broad tunability of the parameters opens the door to a wide range of exotic phenomena[37].

Our results are fourfold. First, in a 1D chain, using our ability to prepare initial product states and to tune the ratio of tunnelling strength t to magnetic spin interaction J, we observe a dynamical phase separation between holes and spins and examine the properties of repulsively bound hole pairs. Second, we investigate the interplay between NNN tunnelling t' and the perturbative pair tunnelling induced by NN tunnelling t. Depending on the sign of the hole tunnelling t', this leads to constructive or destructive interference, which allows us to control the effective mass of the hole pairs, as well as their mobility. Third, we investigate the influence of the spin background on the mass and binding energy of the pair. Last, we perform single-hole experiments in a 2D array for both a ferromagnetic (FM) and AFM spin background. In particular, in the FM case, we observe the influence of the dipolar tail of the interactions.

Our experimental set-up relies on 1D and 2D arrays of individual ^{87}Rb atoms held in optical tweezers with an intersite spacing a. As shown in Fig. 1a,b, we encode the effective spin-1/2 and the hole in three Rydberg states: $|\downarrow\rangle = |60S_{1/2}, m_J = 1/2\rangle$, $|\uparrow\rangle = |61S_{1/2}, m_J = 1/2\rangle$ and $|h\rangle = |60P_{3/2}, m_J = -1/2\rangle$. The resonant interaction between states of different parity implements dipolar tunnelling with amplitude $t_\sigma \propto (1 - 3\cos^2\theta)$ (ref. 38), in which θ is the angle between the interatomic vector and the quantization axis defined by a 46 G magnetic field, either in the plane of the array (1D case; Fig. 1b,e) or perpendicular to it (2D case) and $\sigma \in \{\uparrow, \downarrow\}$ highlights a slight spin dependence of the hole tunnelling ($t_\uparrow/t_\downarrow \approx 0.95$). In the following, we set $t = (t_\uparrow + t_\downarrow)/2$. The spin–spin interactions arise from the off-diagonal van der Waals interactions $\propto r_{ij}^{-6}$ between the pair states $|60S, 61S\rangle$ (ref. 39), giving rise to AFM XY-type couplings $J_\perp$; also, the diagonal van der Waals interactions between all

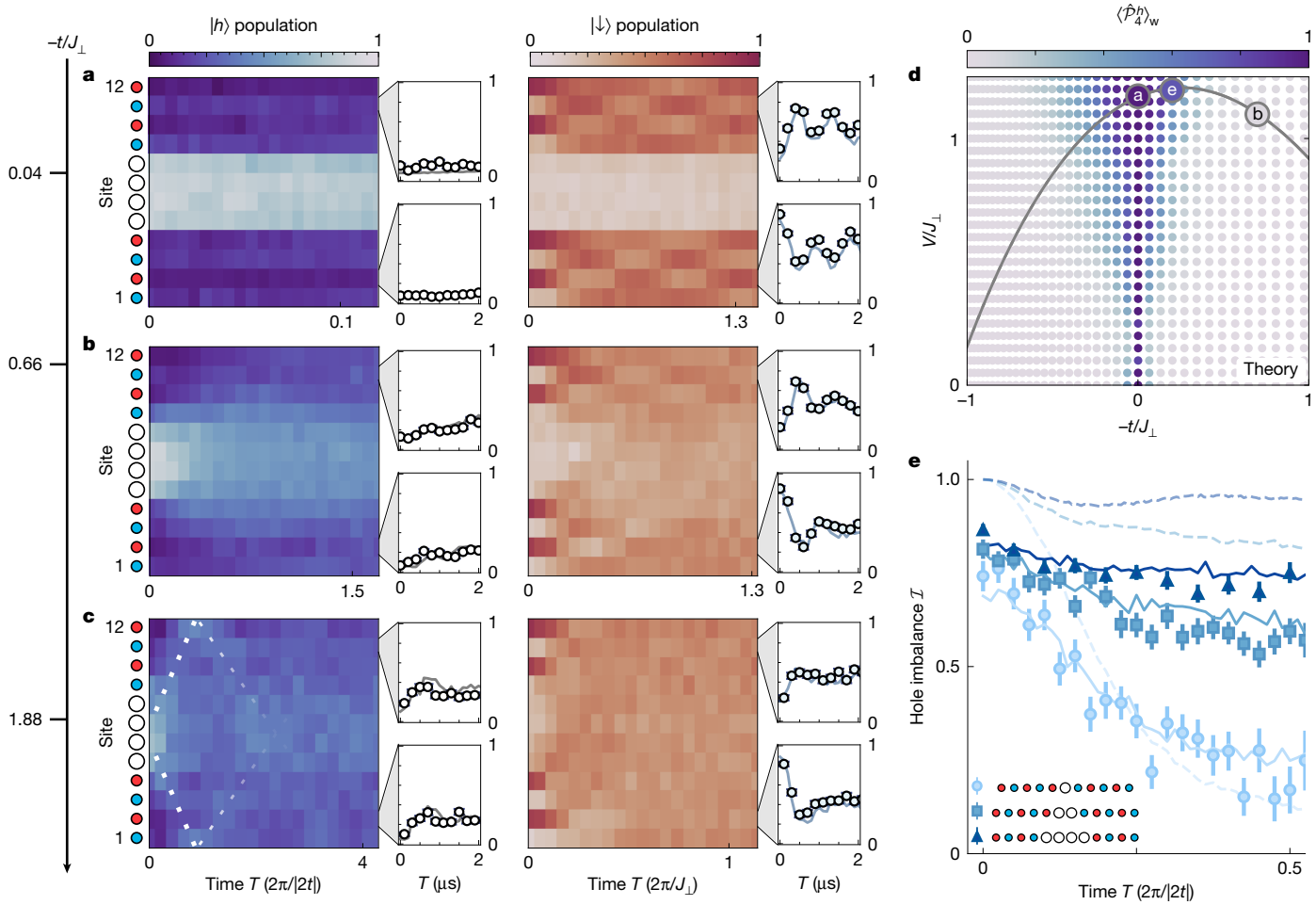

Fig. 2 | Dynamical phase separation in the bosonic *t*–*J*–*V* model. a–**c**, Time evolution of site-resolved $|h\rangle$ (hole) and $|\downarrow\rangle$ (spin down) populations for varying ratios $t/J_\perp$. **a**, $t/J_\perp \approx -0.043(5)$ (measured). **b**, $t/J_\perp \approx -0.66$ (calculated). **c**, $t/J_\perp \approx -1.88$ (calculated). Initial states are indicated by coloured dots in the leftmost column. Insets show population dynamics for selected sites (2nd and 11th), comparing experimental data (points, error bars denote one standard error) with numerical simulations including experiment imperfections (solid lines). **d**, Weighted average of NN four-hole correlations $\langle \hat{P}_4^h \rangle_w$ for the initial state $|\psi_0\rangle = |{\uparrow}{\downarrow}{\uparrow}{\downarrow}hhhh{\uparrow}{\downarrow}{\uparrow}{\downarrow}\rangle$ (see text) as a function of $t/J_\perp$ and $V/J_\perp$, calculated from theory. A value of $\langle \hat{P}_4^h \rangle = 1$ indicates binding of all holes into one cluster. The grey curve shows experimentally accessible parameters through variation of angle θ. **e**, Evolution of the hole imbalance $\mathcal{I}$ for various doping densities (one hole, two holes and four holes; see inset) at $t/J_\perp \approx -0.19$ and $V/J_\perp \approx 1.2$ (corresponding to an angle $\theta = 51.7°$). We postselected experimental data containing hole numbers of 1, 2 and 4, respectively. Solid (dashed) lines are comparisons with numerical simulations including (without) experimental imperfections.

pairs of Rydberg states leads to Ising spin–spin J_z and hole–hole V interactions. The calculated angular dependencies of all of the interactions are non-universal and state-dependent[40] (Fig. 1c). The atomic pair interaction can be expressed in the language of a bosonic *t*–*J*–*V* model given by[5,12]:

$$\begin{aligned}
\hat{H}_{tJV} &= \hat{H}_t + \hat{H}_J + \hat{H}_V, \\
\hat{H}_t &= -\sum_{i<j}\sum_{\sigma=\downarrow,\uparrow} \frac{t_\sigma}{r_{ij}^3}(\hat{a}_{i,\sigma}^\dagger \hat{a}_{j,h}^\dagger \hat{a}_{i,h}\hat{a}_{j,\sigma} + \text{h.c.}), \\
\hat{H}_J &= \sum_{i<j}\frac{1}{r_{ij}^6}\left[J^z \hat{S}_i^z \hat{S}_j^z + \frac{J_\perp}{2}(\hat{S}_i^+ \hat{S}_j^- + \text{h.c.})\right], \\
\hat{H}_V &= \sum_{i<j}\frac{V}{r_{ij}^6}\hat{n}_i^h \hat{n}_j^h.
\end{aligned} \tag{1}$$

in which we have set $\hbar = 1$ and expressed distances r_{ij} in units of the lattice spacing a. The exact mapping contains further boundary terms and spin–hole interactions W that we find to be numerically negligible (see Methods and Extended Data Tables 1 and 2). Although our observations can be qualitatively described by equation (1), we include all terms in our numerical simulations. $\hat{H}_{tJV}$ consists of two parts: $\hat{H}_t + \hat{H}_J$ describes a hard-core bosonic *t*–*J* model and $\hat{H}_V$ represents the hole–hole interaction with interaction strengths $t, J_\perp, J_z$ and V shown in Fig. 1c. The *t*–*J* component comprises a tunnelling term for particles and a magnetic XXZ interaction. The operators $\hat{a}_{j,\sigma}^\dagger$ and $\hat{a}_{j,h}^\dagger$ represent Schwinger bosons that create a spin σ and a hole at site j, respectively. These operators obey bosonic commutation relations for different sites, with an extra hard-core constraint $\sum_\sigma \hat{a}_{j,\sigma}^\dagger \hat{a}_{j,\sigma} + \hat{a}_{j,h}^\dagger \hat{a}_{j,h} = 1$ on each site. We denote the hole density operator at site j by $\hat{n}_j^h = \hat{a}_{j,h}^\dagger \hat{a}_{j,h}$. The spin-1/2 operators $\hat{S}_j^z$ and $\hat{S}_j^\pm = \hat{S}_j^x \pm i\hat{S}_j^y$ at site j only act on the states $|{\uparrow}\rangle$ and $|{\downarrow}\rangle$ with $\hat{S}_j^\gamma = \frac{1}{2}\hat{a}_{j,\alpha}^\dagger \sigma_{\alpha\beta}^\gamma \hat{a}_{j,\beta}$ and Pauli matrices σ^γ ($\gamma = x, y, z$). The Hamiltonian of equation (1) features a $U(1)$ conservation of hole dopants $\hat{N}_h = \sum_j \hat{n}_j^h$ and conserves the total magnetization $\hat{S}_{\text{tot}}^z = \sum_j \hat{S}_j^z$.

In this Rydberg encoding scheme, the tunnelling term exhibits a $1/r^3$ dipolar behaviour, whereas the magnetic spin interaction decays as $1/r^6$. The different power-law scaling of the tunnelling and spin interactions with distance combined with the angular dependence of t allows tuning the ratio $t/J_\perp$ over a wide range (Fig. 1c). At the magic angle $\theta_{ij} \approx 54.7°$, the tunnelling vanishes ($t = 0$), placing the system in the $|t| \ll J_\perp$ regime; increasing the interatomic distance

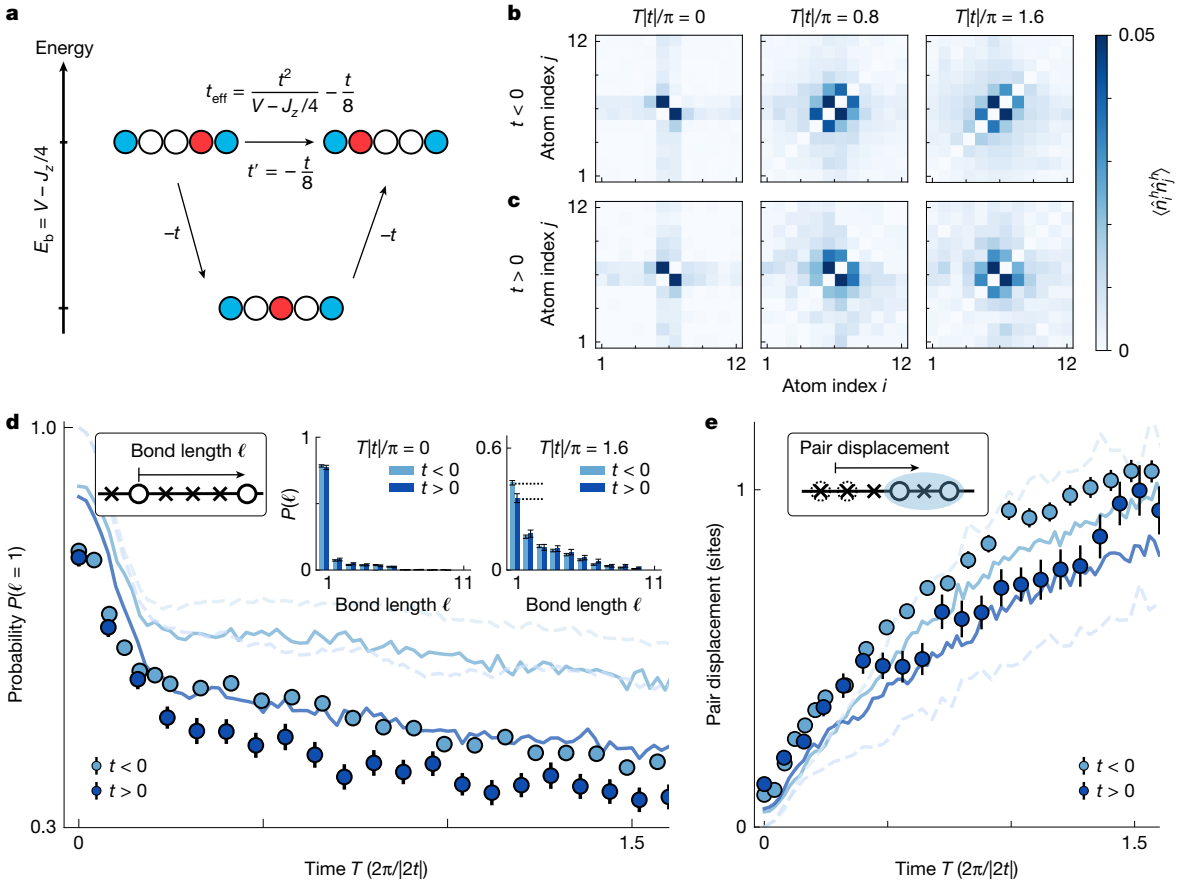

Fig. 3 | Influence of the NNN tunnelling on the dynamics of hole pairs. **a**, Energy diagram illustrating the perturbative tunnelling of bound pairs in a frozen spin background $J_\perp = 0$, in which NN tunnelling contributes $t^2/(V - J_z/4)$ (sign-independent) and NNN tunnelling contributes $t' = -t/8$ (sign-dependent). **b**,**c**, Hole–hole correlations $\langle \hat{n}_i^h \hat{n}_j^h \rangle$ at different times for: $\theta = 49.7°$ ($t < 0$) (**b**) and $\theta = 59.7°$ ($t > 0$) (**c**). **d**, Time evolution of the probability of finding a bound state with bond length $\ell = 1$ for positive ($t > 0$, dark blue) and negative ($t < 0$, light blue) tunnelling. Insets show the distribution of hole–hole separations at $T = 0$ and $T = 4$ μs. **e**, Time evolution of the pair displacement (see inset) for both $t > 0$ and $t < 0$. We restrict the analysis to configurations in which the holes are separated by at most two bonds $\ell \leq 2$. Dots are experimental data, solid lines represent numerical simulations with experimental error and dashed lines are the simulations in the absence of imperfections. Error bars denote one standard error of the mean. All of the data in Fig. 3 are postselected, retaining only experiments containing two holes.

r_{ij} leads to $|t| \gg J_\perp$ owing to the different spatial decay of these interactions. In our experiment, for $a = 9.9$ μm corresponding to the 1D chain studied below, AFM XY interactions with numerically calculated strength $J_\perp = 2\pi \times 692$ kHz coexist with FM Ising interactions $J_z = -2\pi \times 443$ kHz and hole–hole interaction $V = 2\pi \times 819$ kHz at $\theta = 54.7°$. The hole tunnelling amplitude can be tuned between $|t| = 2\pi \times (0 \ldots 1)$ MHz. We have confirmed experimentally the calculated values and angular dependencies of $J_\perp$ and $t_\downarrow$ using pairs of atoms prepared in either a $|\downarrow h\rangle$ or a $|\downarrow\uparrow\rangle$ configuration and observing the corresponding resonant exchange dynamics between the two atoms. The results are summarized in Fig. 1d,e. We discuss the experimental imperfections in Methods and in ref. 39. For all of the many-body experiments reported below, the starting point is a product state, prepared by site-dependent light shifts and microwave rotations (see Methods).

In a first set of experiments, we demonstrate the tunability of the platform by investigating, in a 1D chain, the interplay between spin dynamics and hole propagation in various regimes. To do so, we vary the angle θ of the tweezer chain with respect to the in-plane magnetic field, thus tuning the ratio of tunnelling amplitude t to spin–spin interaction $J_\perp$. We initialize a 12-atom chain in a Néel AFM configuration along z with four holes positioned at its centre: $|\psi_0\rangle = |\uparrow\downarrow\uparrow\downarrow hhhh \uparrow\downarrow\uparrow\downarrow\rangle$ (Fig. 2). For this initial state with a high energy density, we expect dynamics of both holes and spins.

We then suddenly turn off the light shift, let the system evolve freely under $\hat{H}_{tJV}$ and measure the evolution of the state as a function of time. Figure 2a–c presents the time evolution of the hole density $\langle \hat{n}_i^h \rangle$ and the spin density $\langle \hat{n}_i^\downarrow \rangle$ for three angles. Close to the magic angle $\theta = 54.7°$ (Fig. 2a), in which $|t/J_\perp| \ll 1$ (experimentally, $|t| = 2\pi \times 30(10)$ kHz), we observe a separation of hole and spin domains. The holes, initially prepared in the centre, form a static domain that remains separated from the surrounding spins. This situation exhibits minimal hole diffusion while still featuring coherent spin oscillations. We compare the results with numerical simulations including experimental imperfections (see Methods), finding good agreement between the two. Using this simulation, we extrapolate that the separation of spin and charge domains survives up to times T longer than that achieved experimentally. When we decrease θ to 45° ($t/J_\perp \approx -0.66$, $V/J_\perp \approx 1.1$; Fig. 2b), we still measure substantial occupation of the holes on their initial sites, although the domain wall begins to destabilize. Concurrently, we observe damped spin oscillations in the region in which holes partially penetrate. Further reducing θ to 30° ($t/J_\perp \approx -1.88$, $V/J_\perp \approx -0.18$) greatly alters the behaviour of the holes, as seen in Fig. 2c. In this strong tunnelling regime, holes rapidly delocalize across the entire chain and are reflected at the boundary, as highlighted by the dotted lines in Fig. 2c (guide to the eye). The spin dynamics become erratic, indicating that magnetic order is suppressed by the motion of the holes.

To understand the origin of the initial phase separation between hole-rich and spin-rich regions, we need to consider the interplay between the processes described by $t, J_\perp, J_z$ and V. In the limit of small tunnelling $|t/J_z| \ll 1$ and $J_\perp = V = 0$, we expect a trivial binding owing to the energy cost $|J_z/4|$ of breaking a spin bond (we call the bond-breaking cost the binding energy). In the presence of spin fluctuations $J_\perp$ but no hole–hole interaction ($V = 0$), the hole cluster can be destabilized when the binding energy is absorbed by the spin background, especially for large system sizes. The observation of a stable phase separation points towards the stabilizing role of the hole–hole interaction V. To analyse this, we calculate the eigenstates $\{|n\rangle\}$ of the chain (equation (12), see Methods) for various values of $V/J_\perp$ and introduce a projector $\hat{\mathcal{P}}_4^h = \sum_j \hat{n}_j^h \hat{n}_{j+1}^h \hat{n}_{j+2}^h \hat{n}_{j+3}^h$ that extracts the hole-rich contribution of each eigenstate independent of the spin background. The weighted overlap $\langle \hat{\mathcal{P}}_4^h \rangle_w = \sum_n |\langle n|\psi_0\rangle|^2 \langle n|\hat{\mathcal{P}}_4^h|n\rangle$ with our initial state $|\psi_0\rangle$ is directly related to the diagonal ensemble, that is, the expectation value $\langle \hat{\mathcal{P}}_4^h \rangle$ after equilibration. The results are shown in Fig. 2d, in which we observe that the range of $t/J_\perp$ for which we expect the dynamical phase separation increases with hole–hole repulsion. This can be further understood by the effective mass of a cluster of holes. For instance, a repulsively bound pair[41] of adjacent holes $|..\downarrow\uparrow hh\downarrow\uparrow..\rangle$ can only propagate through a second-order process in which the pair temporarily breaks apart: one hole tunnels (amplitude t), followed by the breaking of a nearby $\uparrow,\downarrow$ pair (energy cost $V - J_z/4$) and subsequent recombination, resulting in an effective tunnelling amplitude $t^2/(V - J_z/4)$. Extending to a four-hole bound state, the hole cluster moves by a fourth-order perturbative process $\propto t^4/(V - J_z/4)^3$. Therefore, as system size increases, while keeping the density of holes fixed, we expect an increasingly heavy cluster of holes with a slower propagation.

To confirm this experimentally, we study the dynamics of one-hole, two-hole and four-hole initial states at fixed $t/J_\perp \approx -0.19$ and $V/J_\perp \approx 1.2$. To this end, we quantify the spatial separation between hole-rich and hole-free regions by the hole imbalance:

$$\mathcal{I} = \frac{1}{N_{\text{hole}}} \sum_{i \in A} \langle \hat{n}_i^h \rangle - \frac{1}{L - N_{\text{hole}}} \sum_{j \notin A} \langle \hat{n}_j^h \rangle, \qquad (2)$$

in which N_{hole} is the number of holes, L is the number of sites and A denotes the sites initially occupied by holes. Figure 2e compares the time evolution of $\mathcal{I}$ for systems with $N_{\text{hole}} = 1, 2$ and 4. The data reveal a slowdown in the melting of the boundary between hole-rich and hole-free regions as the number of holes increases from the single-hole case in which the dynamics is purely governed by the tunnelling amplitude t, in agreement with our numerical simulations.

This study of phase separation exemplifies the tunability of the platform, enabling the investigation of previously inaccessible parameter regimes and initial states[42]. Our findings constitute an important step towards understanding phase separation that is found to compete with stripe order and the pseudogap in cuprate superconductors[43] and is relevant to a broader class of strongly correlated electron systems, such as magnetic oxides[44]. Early numerical studies in hard-core bosonic t–J models have further revealed phase separation[29], pointing towards a common underlying mechanism in doped antiferromagnets. Our comparison of two-hole and four-hole clusters shows that, in the limit $J, V \gg t$, the pairing of holes may occur as a precursor to phase separation.

The perturbative argument presented above for the mobility of a two-hole bound state neglects the fact that the tunnelling amplitude t results from a dipolar interaction allowing for direct, NNN tunnelling t' of one of the holes constituting the pair across the other hole, as represented in Fig. 3a. The propagation of the bound pair from one site thus results from the interference between the second-order coupling described above and the direct tunnelling with amplitude $t' = t/8$. This leads to an effective tunnelling amplitude of the bound pair $t_{\text{eff}} = \chi t^2/(V - J_z/4) - t/8$, in which $\chi = \chi(T)$ is a time-dependent prefactor describing the spin fluctuations (see Methods). Depending on the sign of t, the interference can be destructive or constructive, allowing us to tune the mass of the pair $m_{\text{eff}} \propto 1/(2t_{\text{eff}})$ by varying the angle θ. To lowest order in t, the binding energy $E_b = V - J_z/4$ in our perturbative description is unaffected by the interference with NNN tunnellings t'.

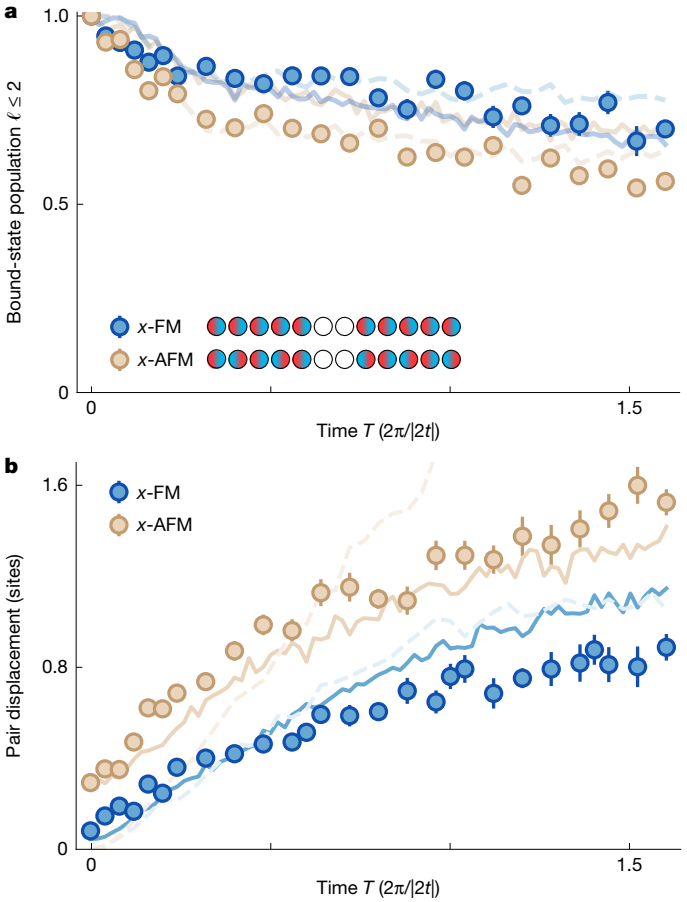

Fig. 4 | Hole dynamics in different magnetic spin backgrounds. a, Time evolution of the probability of finding two holes within two bonds of each other ($\ell \leq 2$) for FM (x-FM, blue) and AFM (x-AFM, brown) spin backgrounds, normalized to the value at time $T = 0$ to compensate for state-preparation errors. **b**, Time evolution of the pair displacement defined as in the caption of Fig. 3d. Solid (dashed) lines show numerical simulations including (without) experimental imperfections in **a** and **b**. Error bars denote one standard error of the mean.

To reveal the effect of the tunnelling's dipolar tail in the propagation of a bound pair, we analyse the dynamics for two different signs of t, controlled by the angle θ. We choose two values of $\theta = 49.7°$ and 59.7°, corresponding respectively to ($t/J_\perp = -0.32$, $V/J_\perp = 1.2$) and ($t/J_\perp = 0.29$, $V/J_\perp = 1.0$). We plot in Fig. 3b ($t < 0$) and Fig. 3c ($t > 0$) the non-connected hole–hole correlations $\langle \hat{n}_i^h \hat{n}_j^h \rangle$ following the preparation of a pair hh at the centre of the chain, after an evolution time $T = 2$ μs ($T = 0.8 \times \frac{2\pi}{|2t|}$) and 4 μs ($T = 1.6 \times \frac{2\pi}{|2t|}$). From the correlation maps, we observe that the pair remains essentially bound during the time evolution, as correlations propagate mainly along the diagonal. We also see that, for $t < 0$ ($\theta = 49.7°$), the bound pair spreads along the first diagonal of the correlation map (thin, long ellipse), whereas for $t > 0$ ($\theta = 59.7°$), the correlations spread slower and also along the second diagonals (fat, short ellipse), suggesting different binding strengths and delocalization speeds of the hole pairs.

To quantify these observations, we first plot in the inset of Fig. 3d the histogram of the distance between the two holes (bond length), at the initial time $T = 0$ and after a time $T = 1.6 \times \frac{2\pi}{|2t|}$. As the probability of the bond length $\ell = 1$ at $T = 1.6 \times \frac{2\pi}{|2t|}$ is higher for $t < 0$ than $t > 0$, the binding is slightly tighter for the first case because V is coincidentally stronger for $t < 0$. This is consistent with the fact that the calculated

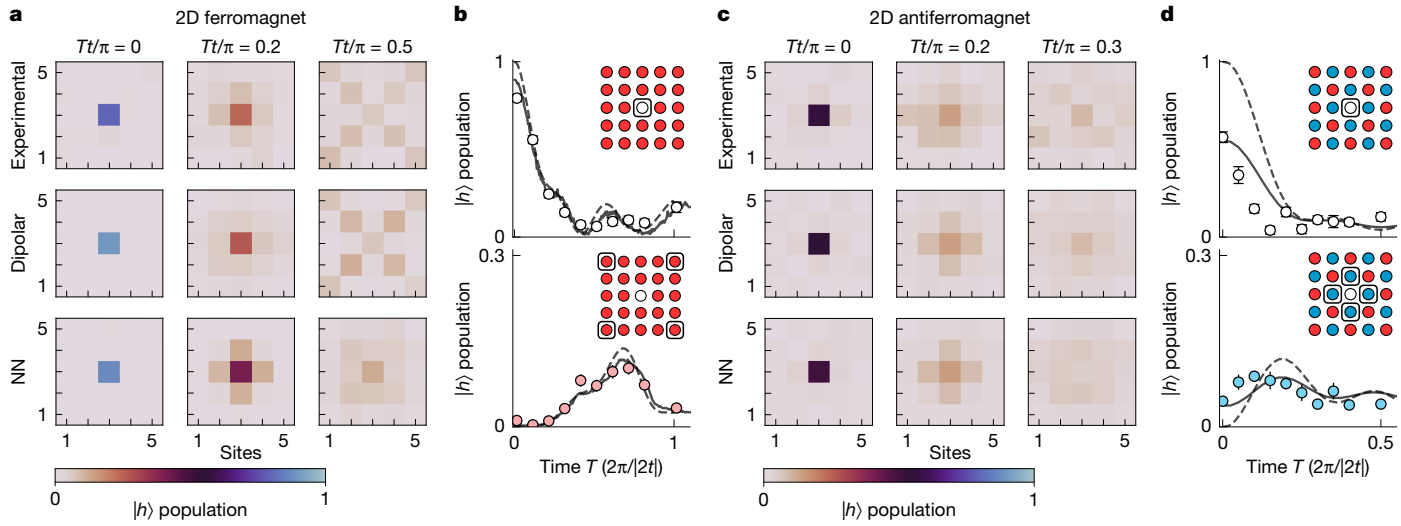

Fig. 5 | Hole dynamics in 2D quantum magnets. a, Spatial maps of the hole probability at various evolution times T for a hole initialized in the 2D ferromagnet spin background $|{\downarrow}\rangle$. The top row shows the experimental data, the middle row is a numerical simulation with the dipolar couplings of the Rydberg interactions and the bottom row considers the theoretical case of NN interactions. **b**, Time evolution of the hole probability at the initial centre site (top) and at a corner site (bottom). Solid lines (dashed lines) are simulations with (without) experimental imperfections. **c**,**d**, Same as **a**,**b** but in the case of an antiferromagnet spin background along z. The bottom panel in **d** now shows the hole population in a NN site to the initial position.

binding energy $E_b = V + |J_z|/4$ (see Methods) is lower in the first case: $E_b = 2\pi \times 0.91$ MHz for $t < 0$ and $E_b = 2\pi \times 0.85$ MHz for $t > 0$. Figure 3d shows that the bond length $\ell = 1$ probability remains larger for the tightly bound pair than for the weakly bound pair throughout experimentally accessible times. We find that the numerical simulations using single-site state-preparation errors qualitatively but not quantitatively describe the experimental data, possibly because of correlated errors in the initial state not included in the simulations (see Methods).

Second, we characterize the pair mobility by measuring their centre-of-mass displacement, defined as the distance between the final and initial centre-of-mass positions. Here we define the pairs as holes with bond length $\ell \leq 2$, to distinguish the bound state from the single-particle background of the bimodal distribution visible in the histograms in Fig. 3d at $T = 1.6 \times \frac{2\pi}{|2t|}$. The results are shown in Fig. 3e and feature the expected asymmetry. They are also in qualitative (quantitative) agreement with numerical simulations without (with) errors. From Fig. 3d,e, we conclude that pairs are lighter (heavier) and less (more) extended for $t < 0$ ($t > 0$). This behaviour is a direct consequence of the $1/r^3$ tail in the tunnelling amplitude of the holes and would be absent for NN interactions. In particular, for NN interactions, the hole pairs would have the same mass $m_{\mathrm{eff}} \propto 1/(2t_{\mathrm{eff}})$ according to the perturbative argument above.

In a last experiment in 1D, we investigate how different magnetic backgrounds influence the dynamics of the hole pairs. Specifically, we address two questions: does the spin background modify whether the pair remains bound and, if yes, how do the holes propagate? From the perturbative description of the bound pair, we infer that the binding energy and effective mass can be tuned by changing the spin contribution to the energy of the initial state. In particular, the binding energy $E_b = V \pm J_\alpha/4$ depends on the relative orientation of spins (±) and direction ($J_\alpha = J_z, J_\perp$). To examine this effect and investigate the influence of $J_\perp$, we use a chain at $\theta = 49.7°$ and prepare two distinct spin configurations, now along x: an AFM Néel order (x-AFM, $|{\leftarrow}{\rightarrow}{\leftarrow}{\rightarrow}{\leftarrow}hh{\rightarrow}{\leftarrow}{\rightarrow}{\leftarrow}{\rightarrow}\rangle$) and a FM state ($x$-FM, $|{\leftarrow}{\leftarrow}{\leftarrow}{\leftarrow}{\leftarrow}hh{\leftarrow}{\leftarrow}{\leftarrow}{\leftarrow}{\leftarrow}\rangle$). We again initialize two holes at the centre and track the time evolution of their position. We first investigate the binding of holes by analysing their separation distance, defining bound pairs as those separated by at most two bonds $\ell \leq 2$. The holes remain bound in both magnetic backgrounds owing to hole–hole interaction V, although slightly weaker in the x-AFM case, as shown in Fig. 4a. We find better agreement with ideal simulations, again indicating that our error model does not capture all experimental imperfections.

Next we characterize the pair mobility by measuring the pair displacement. The results, shown in Fig. 4b, reveal that bound pairs propagate much faster in the x-AFM background compared with the x-FM case, in agreement with our numerical simulations. This behaviour is consistent with the effective pair tunnelling amplitude $\propto 1/(V \mp J_\perp/4)$ for x-AFM (−) and x-FM (+) backgrounds, respectively. Because V and $J_\perp$ have the same sign, the pairs experience weaker binding in the x-AFM case. In contrast to the tightly bound, light pair and weakly bound, heavy pair revealed in Fig. 3, here we observe a tightly bound, heavy pair and a weakly bound, light pair.

Finally, we extend our study to investigate the dynamics of a single hole in 2D. Our motivation is twofold. First, we aim at seeing the influence of the dipolar tail of the tunnelling on the dynamics, in the case of a FM background on a square lattice. Second, we demonstrate the ability of the platform to explore the hole dynamics in an AFM background, relevant for the understanding of doped AFM Mott insulators[1,45]. In 2D, although the angular dependence of all couplings is fixed by setting the magnetic field perpendicular to the atomic plane $\theta = 90°$—fixing the ratio $V/J_\perp = -0.07$, $J_z/J_\perp = -0.68$—we can tune the ratio $t/J_{\perp,z}$ by varying the lattice spacing, exploiting the different power laws of tunnelling ($\propto r^{-3}$) and spin exchange ($\propto r^{-6}$) interactions. Here we implement a 5×5 square array with spacing $a = 12$ µm and $t/J_\perp = 2$ ($t = 2\pi \times 509$ kHz) and initialize it in a polarized FM or AFM product state along z, with a single hole at the centre.

Figure 5a shows the local hole occupation number in the FM case at two different times. There, the dynamics reduces to that of a single particle (here the hole) tunnelling in a 2D lattice with dipolar $\propto t/r^3$ tunnelling rate. The observed coherent evolution of the hole shows a distinctive interference pattern, which is a fingerprint of the associated band structure: in particular, the hole occupation exhibits pronounced peaks at $T = 0.5 \times \frac{2\pi}{|2t|}$ ($T = 0.515$ µs) along the diagonal of the 2D array, a feature absent in the simulation including only NN interactions. Figure 5b focuses on the evolution of the hole occupation at the centre and corner of the array and compares simulations including experimental errors (solid lines) to the ideal simulations (dashed lines) with dipolar tails.

The AFM case is presented in Fig. 5c. There we expect that the paths of the hole do not interfere because of their different spin backgrounds that keep memory of the trajectory[45]. Furthermore, the initial AFM state allows for strong fluctuations in both the charge (that is, the hole) and spin sector owing to tunnelling t and spin flip-flop processes $J_\perp$. In Fig. 5d, we compare the evolution of the hole occupation with time-dependent matrix product state simulations to ideal (dashed lines) and error (solid lines) simulations incorporating measured state-preparation infidelities (see Methods). The error simulations (solid lines) are in good agreement with our experiment, by comparing the peak at the centre and its adjacent sites at early evolution times; at later times, both the numerical simulations and the experiment become featureless owing to the high-energy initial state prepared in the experiment. The AFM spin background makes different paths distinguishable; consequently, interference between these paths is suppressed, leading to a damped revival at the initial hole position. In future experiments, an adiabatic evolution starting from a staggered spin pattern—as demonstrated for the 2D square lattice[46]—will allow us to investigate the low-energy properties of holes in the t–J model.

In summary, we have realized 1D and 2D doped quantum magnets in a Rydberg tweezer array, implementing a fully tunable t–J–V model by mapping three Rydberg states to pseudo-spins and holes[12]. We demonstrated the tunability of the interaction strength, the formation of repulsively bound holes and how the NNN tunnelling affects the perturbative tunnelling of bound pairs in 1D. Finally, we showed that the experiment can explore the 2D case, enabling us to examine the interplay between doping, spin ordering[29,32,33] and frustration in a variety of geometries[13], such as ladders[36]. This demonstration of the use of three Rydberg states is a first step towards the exploration of the physics of spin-1 chains and Haldane phases[14].

Online content

Any methods, additional references, Nature Portfolio reporting summaries, source data, extended data, supplementary information, acknowledgements, peer review information; details of author contributions and competing interests; and statements of data and code availability are available at https://doi.org/10.1038/s41586-025-09377-1.

1. Lee, P. A., Nagaosa, N. & Wen, X.-G. Doping a Mott insulator: physics of high-temperature superconductivity. *Rev. Mod. Phys.* **78**, 17–85 (2006).
2. Bohrdt, A., Homeier, L., Reinmoser, C., Demler, E. & Grusdt, F. Exploration of doped quantum magnets with ultracold atoms. *Ann. Phys.* **435**, 168651 (2021).
3. Auerbach, A. *Interacting Electrons and Quantum Magnetism* (Springer, 1994).
4. Carroll, A. N. et al. Observation of generalized *t*-*J* spin dynamics with tunable dipolar interactions. *Science* **388**, 381–386 (2025).
5. Gorshkov, A. V. et al. Tunable superfluidity and quantum magnetism with ultracold polar molecules. *Phys. Rev. Lett.* **107**, 115301 (2011).
6. Qin, M. et al. Absence of superconductivity in the pure two-dimensional Hubbard model. *Phys. Rev. X* **10**, 031016 (2020).
7. Jiang, H.-C. & Devereaux, T. P. Superconductivity in the doped Hubbard model and its interplay with next-nearest hopping *t*′. *Science* **365**, 1424–1428 (2019).
8. Jiang, Y.-F., Devereaux, T. P. & Jiang, H.-C. Ground-state phase diagram and superconductivity of the doped Hubbard model on six-leg square cylinders. *Phys. Rev. B* **109**, 085121 (2024).
9. Xu, H. et al. Coexistence of superconductivity with partially filled stripes in the Hubbard model. *Science* **384**, eadh7691 (2024).
10. Bespalova, T. A., Delić, K., Pupillo, G., Tacchino, F. & Tavernelli, I. Simulating the Fermi-Hubbard model with long-range hopping on a quantum computer. *Phys. Rev. A* **111**, 052619 (2025).
11. Bohrdt, A. et al. Microscopy of bosonic charge carriers in staggered magnetic fields. Preprint at https://arxiv.org/abs/2410.19500 (2024).
12. Homeier, L. et al. Antiferromagnetic bosonic *t*–*J* models and their quantum simulation in tweezer arrays. *Phys. Rev. Lett.* **132**, 230401 (2024).
13. Browaeys, A. & Lahaye, T. Many-body physics with individually controlled Rydberg atoms. *Nat. Phys.* **16**, 132–142 (2020).
14. Mögerle, J. et al. Spin-1 haldane phase in a chain of Rydberg atoms. *PRX Quantum* **6**, 020332 (2025).
15. Liu, V. S. et al. Supersolidity and simplex phases in spin-1 Rydberg atom arrays. Preprint at https://arxiv.org/abs/2407.17554 (2024).
16. Scalapino, D. J. A common thread: the pairing interaction for unconventional superconductors. *Rev. Mod. Phys.* **84**, 1383–1417 (2012).
17. Proust, C. & Taillefer, L. The remarkable underlying ground states of cuprate superconductors. *Annu. Rev. Condens. Matter Phys.* **10**, 409–429 (2019).
18. Bednorz, J. G. & Müller, K. A. Possible highT_c superconductivity in the Ba–La–Cu–O system. *Z. Phys. B Condensed Matter* **64**, 189–193 (1986).
19. Keimer, B., Kivelson, S. A., Norman, M. R., Uchida, S. & Zaanen, J. From quantum matter to high-temperature superconductivity in copper oxides. *Nature* **518**, 179–186 (2015).
20. Bloch, I., Dalibard, J. & Zwerger, W. Many-body physics with ultracold gases. *Rev. Mod. Phys.* **80**, 885–964 (2008).
21. Mazurenko, A. et al. A cold-atom Fermi–Hubbard antiferromagnet. *Nature* **545**, 462–466 (2017).
22. Shao, H.-J. et al. Antiferromagnetic phase transition in a 3D fermionic Hubbard model. *Nature* **632**, 267–272 (2024).
23. Hirthe, S. et al. Magnetically mediated hole pairing in fermionic ladders of ultracold atoms. *Nature* **613**, 463–467 (2023).
24. Lebrat, M. et al. Observation of Nagaoka polarons in a Fermi–Hubbard quantum simulator. *Nature* **629**, 317–322 (2024).
25. Prichard, M. L. et al. Directly imaging spin polarons in a kinetically frustrated Hubbard system. *Nature* **629**, 323–328 (2024).
26. Duan, L.-M., Demler, E. & Lukin, M. D. Controlling spin exchange interactions of ultracold atoms in optical lattices. *Phys. Rev. Lett.* **91**, 090402 (2003).
27. Gross, C. & Bloch, I. Quantum simulations with ultracold atoms in optical lattices. *Science* **357**, 995–1001 (2017).
28. Emery, V. J., Kivelson, S. A. & Lin, H. Q. Phase separation in the *t*-*J* model. *Phys. Rev. Lett.* **64**, 475 (1990).
29. Boninsegni, M. Phase separation in mixtures of hard core bosons. *Phys. Rev. Lett.* **87**, 087201 (2001).
30. Sun, H. et al. Realization of a bosonic antiferromagnet. *Nat. Phys.* **17**, 990–994 (2021).
31. Jepsen, P. N. et al. Transverse spin dynamics in the anisotropic Heisenberg model realized with ultracold atoms. *Phys. Rev. X* **11**, 041054 (2021).
32. Harris, T. J., Schollwöck, U., Bohrdt, A. & Grusdt, F. Kinetic magnetism and stripe order in the doped AFM bosonic *t*–*J* model. Preprint at https://arxiv.org/abs/2410.00904v1 (2024).
33. Zhang, H.-K., Zhang, J.-X., Xu, J.-S. & Weng, Z.-Y. Quantum-interference-induced pairing in antiferromagnetic bosonic *t*-*J* model. Preprint at https://arxiv.org/abs/2409.15424 (2024).
34. Siller, T., Troyer, M., Rice, T. M. & White, S. R. Bosonic model of hole pairs. *Phys. Rev. B* **63**, 195106 (2001).
35. O'Mahony, S. M. et al. On the electron pairing mechanism of copper-oxide high temperature superconductivity. *Proc. Natl. Acad. Sci.* **119**, e2207449119 (2022).
36. Morera, I., Bohrdt, A., Ho, W. W. & Demler, E. Attraction from kinetic frustration in ladder systems. *Phys. Rev. Res.* **6**, 023196 (2024).
37. Sous, J. & Pretko, M. Fractons from polarons. *Phys. Rev. B* **102**, 214437 (2020).
38. Barredo, D. et al. Coherent excitation transfer in a spin chain of three Rydberg atoms. *Phys. Rev. Lett.* **114**, 113002 (2015).
39. Emperauger, G. et al. Benchmarking direct and indirect dipolar spin-exchange interactions between two Rydberg atoms. *Phys. Rev. A* **111**, 062806 (2025).
40. Wadenpfuhl, K. & Adams, C. S. Unravelling the structures in the van der Waals interactions of alkali Rydberg atoms. *Phys. Rev. A* **111**, 062803 (2025).
41. Winkler, K. et al. Repulsively bound atom pairs in an optical lattice. *Nature* **441**, 853–856 (2006).
42. Staszewski, L. & Wietek, A. Quench dynamics of stripes and phase separation in the two-dimensional *t*-*J* model. *Phys. Rev. B* **112**, 035125 (2025).
43. White, S. R. & Scalapino, D. J. Phase separation and stripe formation in the two-dimensional *t*–*J* model: a comparison of numerical results. *Phys. Rev. B* **61**, 6320 (2000).
44. Kagan, M. Y., Kugel, K. I. & Rakhmanov, A. L. Electronic phase separation: recent progress in the old problem. *Phys. Rep.* **916**, 1–105 (2021).
45. Ji, G. et al. Coupling a mobile hole to an antiferromagnetic spin background: transient dynamics of a magnetic polaron. *Phys. Rev. X* **11**, 021022 (2021).
46. Chen, C. et al. Continuous symmetry breaking in a two-dimensional Rydberg array. *Nature* **616**, 691–695 (2023).

Methods

Experimental set-up

Our implementation of the t–J–V model is based on the following mapping: $|\downarrow\rangle = |60S_{1/2}, m_J = 1/2\rangle$, $|\uparrow\rangle = |61S_{1/2}, m_J = 1/2\rangle$ and $|h\rangle = |60P_{3/2}, m_J = -1/2\rangle$. We use a 46 G quantization magnetic field that is oriented in the atomic plane of the optical tweezers. The resonant microwave frequencies of the transitions $|\downarrow\rangle \leftrightarrow |h\rangle$ and $|h\rangle \leftrightarrow |\uparrow\rangle$ are 17,179 and 17,675 MHz, respectively. All microwave pulses are emitted by antennas placed outside the vacuum chamber.

We use two 1,014-nm lasers to generate site-resolved light shifts, respectively on the states $|\downarrow\rangle$ and $|\uparrow\rangle$. One laser is blue-detuned by 300 MHz from the transition between the intermediate state $|6P_{3/2}\rangle$ and $|\downarrow\rangle$, resulting in a light shift $\delta_\downarrow \approx -2\pi \times 40$ MHz on the state $|\downarrow\rangle$; the local control is achieved by diffraction on a spatial light modulator. Another laser is red-detuned by 200 MHz from the transition $|6P_{3/2}\rangle$ and $|\uparrow\rangle$, creating a light shift $\delta_\uparrow \approx 2\pi \times 30$ MHz on the state $|\uparrow\rangle$; it is diffracted on an acousto-optical modulator.

State initialization

Atoms are randomly loaded into an array of optical tweezers with a probability of about 50% and then rearranged by a single moving tweezer generated by a 2D acousto-optical deflector. After the rearrangement, we sequentially use optical molasses and Raman sideband cooling to lower the temperature of the atoms. Then the atoms are optically pumped to $|g\rangle = |5S_{1/2}, F = 2, m_F = 2\rangle$ by means of a σ^+-polarized 795-nm laser. Before the Rydberg excitation, the tweezer depth is adiabatically ramped down by a factor of roughly 4 to reduce the momentum dispersion of the atomic wavefunctions. We then switch off the tweezers and use a two-photon stimulated Raman adiabatic passage (STIRAP) with 420-nm and 1,014-nm lasers to excite all atoms to $|\downarrow\rangle$.

Extended Data Fig. 1 shows a typical Rydberg sequence for the preparation of a doped AFM state along z. We define three classes of sites: the sites in which we want to initialize an atom in $|\uparrow\rangle$ are addressed by the $\delta_\downarrow$ laser; the ones in which we want an atom in $|h\rangle$ are addressed by both the $\delta_\downarrow$ and $\delta_\uparrow$ lasers; and the ones in which we want an atom in $|\downarrow\rangle$ are not addressed. First, we apply a 18-ns microwave π-pulse to bring all of the atoms from $|\downarrow\rangle$ to $|h\rangle$ (all microwave pulses have a Gaussian envelope and their duration is given as their standard deviation multiplied by $\sqrt{2\pi}$). Second, we switch on the light shifts $\delta_\downarrow$ and apply a 36-ns microwave π-pulse on resonance with the bare $|h\rangle \leftrightarrow |\downarrow\rangle$ transition. This transfers the non-addressed atoms from $|h\rangle$ back to $|\downarrow\rangle$, while the addressed atoms remain in $|h\rangle$. Third, we switch on the light shifts $\delta_\uparrow$ and apply a 38-ns microwave π-pulse on resonance with the bare $|h\rangle \leftrightarrow |\uparrow\rangle$ transition. Finally, we simultaneously switch off both light shifts on $|\uparrow\rangle$ and $|\downarrow\rangle$ and let the system evolve under the t–J–V Hamiltonian.

To prepare a doped FM state along z, we remove the third microwave pulse and the light shifts $\delta_\uparrow$ and shine the light shift $\delta_\downarrow$ on the site in which we want to prepare a hole. This results in the initialization of holes ($|h\rangle$) on addressed sites and spins down ($|\downarrow\rangle$) on non-addressed sites.

Finally, to prepare a doped magnet along x, we first prepare a doped magnet along z and then apply a π/2 rotation around y between the states $|\downarrow\rangle$ and $|\uparrow\rangle$. This rotation is achieved through a two-photon microwave pulse with effective Rabi frequency $2\pi \times 9$ MHz, using an intermediate state detuning of about 200 MHz from both $60P_{1/2}$ and $60P_{3/2}$ states.

State detection

Our readout sequence is based on the mapping of one Rydberg state to the ground-state manifold $5S_{1/2}$, which is then imaged by fluorescence. For example, to measure the population in the Rydberg state $|\downarrow\rangle$, we apply an approximately 2.5 μs pulse of 1,014-nm light that deexcites $|\downarrow\rangle$ to the ground-state manifold by means of the short-lived intermediate state $|6P_{3/2}\rangle$. After that, we switch the tweezers back on, to recapture the atoms in the ground-state manifold while expelling the ones in Rydberg states by means of the ponderomotive force. We then image the recaptured atoms in their ground state with site-resolved fluorescence. A recaptured atom is then interpreted as $|\downarrow\rangle$; a lost atom means that the atom is in one of the two remaining states $|h\rangle$ or $|\uparrow\rangle$.

To measure the hole ($|h\rangle$) population, we add a microwave π-pulse before the deexcitation pulse, exchanging the populations of $|h\rangle$ and $|\downarrow\rangle$, and we map the recaptured atoms to $|h\rangle$.

The duration of the deexcitation is on the same order of magnitude as the typical interaction times $2\pi/J_\perp \approx 1.5$ μs. To prevent unwanted dynamics during the readout, we implement a two-step freezing protocol: (1) a three-photon transition at 7.5 GHz with a duration of 70 ns shelves the $|60P_{3/2}, m_J = -1/2\rangle$ population to $|58G\rangle$ and (2) a microwave π-pulse transfers the atoms in $|\uparrow\rangle$ to $|61P_{3/2}, m_J = 3/2\rangle$, which has negligible interaction with $|\downarrow\rangle$. The atomic transitions involved in the freezing scheme are represented as yellow arrows in Extended Data Fig. 1a. Those freezing pulses are applied successively just before the deexcitation.

Error budget: state preparation and detection

To calibrate the initial state-preparation errors, we perform three measurements: one for the ground-state population p_g^{meas}, one for the $|\downarrow\rangle$-state population $p_\downarrow^{\mathrm{meas}}$ and one for the $|h\rangle$-state population p_h^{meas}. Those measurements are performed using the sequence explained in the previous section (to measure p_g^{meas}, we simply remove the deexcitation pulse).

We then estimate the actual populations $p_{g,\downarrow,h,\uparrow}^{\mathrm{act}}$ in the states $|g\rangle$, $|\downarrow\rangle$, $|h\rangle$ and $|\uparrow\rangle$ by correcting for detection errors (this correction is only applied to the data used in the numerical simulations; the experimental data shown in the main text still correspond to the raw data). Our error model for detection errors assumes independent errors that depend on the measurement sequence. The error tree associated to each of the three measurement sequences is shown in Extended Data Fig. 2. To the first order, the effect of the detection errors is

$$\begin{bmatrix} p_g^{\mathrm{meas}} \\ p_\downarrow^{\mathrm{meas}} \\ p_h^{\mathrm{meas}} \end{bmatrix} = M_{\mathrm{err}} \begin{bmatrix} p_g^{\mathrm{act}} \\ p_\downarrow^{\mathrm{act}} \\ p_h^{\mathrm{act}} \\ p_\uparrow^{\mathrm{act}} \end{bmatrix} \quad (3)$$

$$\text{with } M_{\mathrm{err}} = \begin{bmatrix} 1 & \varepsilon_S' & \varepsilon_P' & \varepsilon_S' \\ 1 & 1-\varepsilon & \varepsilon_P' & \varepsilon_S' \\ 1 & \varepsilon_P' & 1-\varepsilon & \varepsilon_S' \end{bmatrix}$$

Here $\varepsilon_S' \approx 5 \pm 1\%$ ($\varepsilon_P' \approx 2 \pm 1\%$) is the probability that an atom initially in $|\downarrow\rangle$ or in $|\uparrow\rangle$ (in $|h\rangle$) decays to the ground state during the measurement, owing to the finite Rydberg lifetimes; $\varepsilon \approx 2 \pm 1\%$ is the probability that an atom in $|\downarrow\rangle$ is lost before the imaging, owing to the finite fidelity of the deexcitation and of the imaging. In equation (3), we do not account for the error of the microwave π-pulse involved in the measurement of p_h^{meas} (denoted by η_{MW} in Extended Data Fig. 2c), as its value strongly depends on the interactions.

To estimate the actual populations, we minimize the following cost function:

$$\left| M_{\mathrm{err}} \begin{bmatrix} p_g^{\mathrm{act}} \\ p_\uparrow^{\mathrm{act}} \\ p_h^{\mathrm{act}} \\ p_\downarrow^{\mathrm{act}} \end{bmatrix} - \begin{bmatrix} p_g^{\mathrm{meas}} \\ p_\uparrow^{\mathrm{meas}} \\ p_h^{\mathrm{meas}} \end{bmatrix} \right|^2 \quad (4)$$

under the constraints $p_g^{\mathrm{act}} + p_\uparrow^{\mathrm{act}} + p_h^{\mathrm{act}} + p_\downarrow^{\mathrm{act}} = 1$, and $p^{\mathrm{act}} \geq 0$. Here we have neglected the residual population in Rydberg states other than $|\downarrow\rangle$, $|h\rangle$ and $|\uparrow\rangle$. We find this maximum likelihood approach to be robust against projection noise.

The estimated state-preparation errors in the initial state after correcting for the detection errors are shown in Extended Data Fig. 3 in the 1D geometry and in Extended Data Fig. 4 in the 2D geometry. We obtain preparation fidelities of 80–95% per site by correcting the measurements at $T = 0$ μs. Those preparation errors arise primarily from three sources: Rydberg interactions during the pulses, STIRAP imperfections (about 2%) and depumping to the ground state caused by the addressing light shifts.

Hamiltonian mapping

The Rydberg Hamiltonian we implement can be mapped exactly to a t–J–V–W model, which we derive in this section. The bare Rydberg Hamiltonian can be written as

$$\hat{H}^{\mathrm{Ryd}} = \sum_{i<j} \hat{H}_{ij}^{\mathrm{Ex},C_3} + \hat{H}_{ij}^{\mathrm{Ex},C_6} + \hat{H}_{ij}^{\mathrm{Diag},C_6}, \tag{5}$$

in which $\hat{H}_{ij}^{\mathrm{Ex},C_3}$ describes the direct dipole–dipole exchange interaction and $\hat{H}_{ij}^{\mathrm{Ex},C_6}$ ($\hat{H}_{ij}^{\mathrm{Diag},C_6}$) are the exchange (diagonal) components of the van der Waals interactions. We express the Hamiltonian in terms of the local Rydberg basis states, that is, an atom on site j is described by the states $\{|60S_j\rangle, |60P_j\rangle, |61S_j\rangle\} \equiv \{|S_j\rangle, |P_j\rangle, |S_j'\rangle\} \equiv \{|\downarrow_j\rangle, |h_j\rangle, |\uparrow_j\rangle\}$. The number operators at site j are thus defined as $\hat{n}_j^{\downarrow} = |\downarrow_j\rangle\langle\downarrow_j|$, $\hat{n}_j^{h} = |h_i\rangle\langle h_j|$ and $\hat{n}_j^{\uparrow} = |\uparrow_j\rangle\langle\uparrow_j|$.

The atomic pair interactions lead to the Hamiltonian in equation (5), which is given by

$$\hat{H}_{ij}^{\mathrm{Ex},C_3} = -\frac{t_{\downarrow}(\theta_{ij})}{r_{ij}^3}(|\downarrow_i, h_j\rangle\langle h_i, \downarrow_j| + \mathrm{h.c.}) \tag{6}$$

$$-\frac{t_{\uparrow}(\theta_{ij})}{r_{ij}^3}(|\uparrow_i, h_j\rangle\langle h_i, \uparrow_j| + \mathrm{h.c.}) \tag{7}$$

and

$$\hat{H}_{ij}^{\mathrm{Ex},C_6} = \frac{J_{\perp}(\theta_{ij})}{2} \times \frac{1}{r_{ij}^6}(|\downarrow_i, \uparrow_j\rangle\langle\uparrow_i, \downarrow_j| + \mathrm{h.c.}) \tag{8}$$

and

$$\hat{H}_{ij}^{\mathrm{Diag},C_6} = \sum_{\alpha,\beta\in\{\downarrow,h,\uparrow\}} \frac{V_{\alpha\beta}(\theta_{ij})}{r_{ij}^6} \hat{n}_i^{\alpha}\hat{n}_j^{\beta}, \tag{9}$$

in which r_{ij} is the vector connecting atoms at sites i and j and θ_{ij} is the angle between the vector r_{ij} and the quantization axis defined by the magnetic field with magnitude $B = 46$ G. The derivation shows that the direct dipole–dipole and the van der Waals exchange interactions are directly related to the tunnelling t and spin flip-flop $J_{\perp}$ (Extended Data Table 1). We emphasize that our choice of Rydberg states only has a small anisotropy in the tunnelling amplitudes $t_{\uparrow}(\theta_{ij}) \approx 0.95 \times t_{\downarrow}(\theta_{ij})$.

Next, we use the hard-core constraint of the Rydberg occupation number, that is,

$$\hat{n}_j^{\downarrow} + \hat{n}_j^{\uparrow} + \hat{n}_j^{h} = 1 \ \forall j, \tag{10}$$

to express the spin-1/2 operators as

$$\begin{aligned} \hat{n}_j^{\downarrow} &= -\hat{S}_j^z + \frac{1}{2} - \frac{1}{2}\hat{n}_j^h \\ \hat{n}_j^{\uparrow} &= +\hat{S}_j^z + \frac{1}{2} - \frac{1}{2}\hat{n}_j^h. \end{aligned} \tag{11}$$

Inserting equation (11) into the diagonal van der Waals Hamiltonian of equation (9) yields

$$\begin{aligned} \hat{H}_{ij}^{\mathrm{Diag},C_6} = {} & \frac{J^z(\theta_{ij})}{r_{ij}^6}\hat{S}_i^z\hat{S}_j^z + \frac{V(\theta_{ij})}{r_{ij}^6}\hat{n}_i^h\hat{n}_j^h \\ & + \frac{W(\theta_{ij})}{r_{ij}^6}(\hat{S}_i^z\hat{n}_j^h + \hat{n}_i^h\hat{S}_j^z) \\ & + \frac{h_j^z(\theta_{ij})}{r_{ij}^6}\hat{S}_j^z - \frac{\mu_j(\theta_{ij})}{r_{ij}^6}\hat{n}_j^h \\ & + \mathrm{const.} \end{aligned} \tag{12}$$

Several of the above terms are neglected in the main text. First, for the chosen atomic levels, the spin–hole interaction W is negligible compared with the other interaction strengths, such as the hole–hole interaction V. Second, the field terms $\propto h_j^z$ and μ_j are mostly flat in the bulk but are different on the boundary, on which an atom in a 1D chain has only one instead of two nearest neighbours. The relations between the couplings in the t–J–V model and the Rydberg Hamiltonian of equation (5) are summarized in Extended Data Table 1.

To obtain the coupling amplitudes of the t–J–V model (see equation (1)), we calculate the atomic pair interactions at magnetic field magnitude $B = 46$ G for angles $\theta_{ij} \in [0, \pi]$ using the pairinteraction software package[47] (see solid markers in Extended Data Fig. 5a). The angular dependence of the van der Waals interactions $\propto C_6^{\alpha\beta}(\theta_{ij})$ can be well fitted by the function $f^{\alpha\beta}(\theta_{ij}) = F_1^{\alpha\beta} + F_2^{\alpha\beta}\cos^2\theta_{ij} + F_3^{\alpha\beta}\cos^4\theta_{ij}$, in which $F_n^{\alpha\beta}$ are fit parameters that depend on the quantum numbers $\alpha,\beta \in \{S, S', P\}$ and the magnitude of the magnetic field. To be explicit, we fit each interaction coefficient $C_6^{\alpha\beta}(\theta_{ij})$ to the function $f^{\alpha\beta}$ (see lines in Extended Data Fig. 5a). We use the extracted $C_6^{\alpha\beta}(\theta_{ij})$ and the calculated $C_3^{\alpha\beta}$ coefficients to determine the interaction strengths at an atomic distance of $a = 9.9$ μm (1D) and $a = 12$ μm (2D) in our numerical simulations; in Fig. 1d–e, we show a comparison of the theoretically calculated and experimentally measured interaction strengths.

The angular dependence of the $C_6^{\alpha\beta}(\theta_{ij})$ and $C_3(\theta_{ij})$ coefficients lead to a strong angular dependence of the couplings in the t–J–V model (Extended Data Table 1). This allows us to tune through a wide parameter regime in the 1D chain by changing the angle between the quantization axis and the unit vector along the chain. In Extended Data Fig. 5b, the interactions $t_{\downarrow}(\theta_{ij})$, $J_z(\theta_{ij})$, $V(\theta_{ij})$ and $W(\theta_{ij})$ at lattice spacing $a = 9.9$ μm are plotted in units of the spin flip-flop interaction $J_{\perp}(\theta_{ij})$; hence, the absolute interaction scale changes from $J_{\perp}(0) = 2\pi \times 507$ kHz to $J_{\perp}(90°) = 2\pi \times 813$ kHz.

We note that the spin–hole interaction $\propto W(\theta_{ij})$ is negligible for the chosen Rydberg states. Thus, we do not expect it to play a role on the timescales of the performed experiments. Nevertheless, because we use the bare Rydberg Hamiltonian for our numerical simulations, all terms including the boundary terms in the Hamiltonian in equation (12) are fully taken into account. We have confirmed the mapping between the bare Rydberg model to the t–J–V model according to Extended Data Table 1 by comparing the full spectra in a small system.

Last, we consider the boundary and field terms that appear in the mapping from Rydberg states to (doped) spin models. They result, in pure spin models, in magnetic field terms h_j^z; in our model, we obtain an extra chemical potential term μ_j. In Extended Data Fig. 6a, we show the spatial dependence of the field terms for the $L = 12$ site chain. In the bulk, the field terms are approximately constant and, because of the particle and magnetization conservation in our model, the field term results in a constant energy shift. However, in the presence of boundaries, on which an atom has only one instead of two nearest neighbours, the field terms are approximately half in magnitude compared with the bulk; hence, these terms only have to be considered at the boundary. In Extended Data Fig. 6b, we further study the difference of the couplings between sites 2 and 1 as we vary the angle θ. In the experiments conducted here, we do not expect the boundary terms to play a substantial role in the physics. For instance, the pair dynamics predominately happens in the bulk. In future experiments

with adiabatic ground-state preparation, the boundaries would have to be considered.

Dynamical phase separation

Ground-state phase separation into hole-rich and hole-free regions have been studied extensively in the fermionic t–J models, particularly in the early years of high-T_c superconductivity[28,48,49], owing to its notion of self-binding of charge carriers. Also, sign-problem-free quantum Monte Carlo studies report phase separation in (partially) AFM bosonic t–J models[29]. The phase separation is found for small values of $|t/J| \ll 1$, in which the kinetic energy is small enough such that the particles cannot escape from the self-bound state. Consequently, in quantum simulation platforms with superexchange-based magnetic interactions, for example, optical lattices, the accessible parameter range does not allow us to examine phase separation.

Although phase separation has previously been studied as a property of the ground state, here we develop a method to dynamically examine phase separation by a quench starting from a product state. We define states with a hole-rich connected-region R as $|\psi\rangle_R = |\psi_s\rangle \otimes \prod_{j\in R} |h\rangle_j$, that is, all N_h holes in the system form a cluster of volume $V(R) = N_h$ and the state $|\psi_s\rangle$ describes the spins located at sites $j \notin R$. To characterize the states $|\Psi\rangle_R$, we consider the projector

$$\hat{\mathcal{P}}^h_{N_h} = \sum_R \prod_{j\in R} \hat{n}^h_j \tag{13}$$

such that the expectation values $\mathcal{P}^h_{N_h} = \langle \hat{\mathcal{P}}^h_{N_h} \rangle$ describe the overlap with hole-rich connected regions. For example, both states $|\uparrow\downarrow\uparrow\downarrow hhhh\uparrow\downarrow\uparrow\downarrow\rangle$ and $|\downarrow\uparrow\uparrow\uparrow\downarrow\downarrow hhhh\uparrow\downarrow\uparrow\rangle$ are assigned the same values $\mathcal{P}^h_4 = 1$ and are therefore labelled as perfectly phase separated by our definition.

Our ansatz is independent of the spin state in the hole-free regions, which is crucial in our analysis because we study far-from-equilibrium states with an energy density well below the highest-energy state; note that the hole–hole repulsion stabilizes phase separation for negative temperature states. In practice, the initial state $|\psi_0\rangle = |\uparrow\downarrow\uparrow\downarrow hhhh\uparrow\downarrow\uparrow\downarrow\rangle$ experiences strong dynamics in the spin sector $|\psi_s\rangle$, whereas the hole-rich sector remains stable throughout the experiment, with some fluctuations at its boundary. Hence, the hole and spin sector seem separated under dynamics.

To quantify whether an initial state $|\psi_0\rangle$ remains phase separated under time evolution, we perform exact diagonalization on the $L = 12$ chain to obtain the entire dynamically accessible spectrum, that is, we fix total magnetization $S^z_{\mathrm{tot}} = 0$ and the number of holes $N_h = 4$. In particular, we calculate the expectation value $\langle n|\ \hat{\mathcal{P}}^h_4\ |n\rangle$ for all eigenstates $|n\rangle$ and define the weighted diagonal ensemble

$$\langle \hat{\mathcal{P}}^h_4 \rangle_{\mathrm{w}} = \sum_n |\langle n|\psi_0\rangle|^2 \langle n|\ \hat{\mathcal{P}}^h_4\ |n\rangle, \tag{14}$$

which we use as an order parameter for dynamical phase separation for the triplet $(\hat{H}, \hat{\mathcal{P}}^h_4, |\psi_0\rangle)$. In fact, the weighted diagonal ensemble is directly related to the infinite time expectation value $\mathcal{P}^h_4(t\to\infty)$ assuming eigenstate thermalization hypothesis:

$$\begin{aligned}\mathcal{P}^h_4(t) &:= \langle\psi(t)|\ \hat{\mathcal{P}}^h_4\ |\psi(t)\rangle \\ &= \sum_{n,m} \langle\psi_0|n\rangle\langle n|\ \hat{\mathcal{P}}^h_4\ |m\rangle\langle m|\psi_0\rangle e^{-i(E_m-E_n)t} \\ &\overset{t\to\infty}{\to} \langle \hat{\mathcal{P}}^h_4 \rangle_{\mathrm{w}}.\end{aligned} \tag{15}$$

The weighted overlap $\langle \hat{\mathcal{P}}^h_4 \rangle_{\mathrm{w}}$ is plotted in Fig. 2d for a hypothetical scan of $t/J_\perp$ and $V/J_\perp$ showing a region in parameter space (dark blue) for which the initial state $|\psi_0\rangle$ equilibrates to a state with a strong character of phase separation. As expected, the hole–hole repulsion V gives rise to a fan-like region around $|t| = 0$ increasing with V.

Influence of magnetic background on hole pair

In the limit of small tunnelling $|t| \ll |J_\perp|, |J_z|, |V|$ studied in our experiments, the qualitative behaviour of the repulsively bound hole pairs can be understood by a perturbative analysis. In fact, the spin background influences both the binding energy E_b of the pair together with the effective mass $m_{\mathrm{eff}} = 1/2t_{\mathrm{eff}}$. Also, the interference of the effective pair tunnelling with the NNN tunnelling process ($\propto \pm t/8$) allows us to tune the mass of the pair by varying the angle θ.

The quench protocol we apply begins from an initial product state at time $T = 0$. At short times, we assume the kinetic motion of holes to be frozen, whereas the spin background evolves under the Hamiltonian in equation (1), allowing us to treat the spin sector independently from the holes in the limit $|J_\perp|, |J_z| \gg |t|$. Under unitary time evolution of a translationally invariant initial spin background, the energy per bond ϵ is conserved and for the four different initial product states given by

$$\begin{aligned}\epsilon_{z\text{-AFM}} &= |J_z|/4 \quad \epsilon_{z\text{-FM}} = -|J_z|/4 \\ \epsilon_{x\text{-AFM}} &= -J_\perp/4 \quad \epsilon_{x\text{-FM}} = J_\perp/4,\end{aligned} \tag{16}$$

in which we neglect boundary terms.

Next, we consider the perturbative tunnelling of a hole pair immersed into the thermalized spin background; here we define the pair to be constituted by neighbouring holes. The energy of the initial state is composed by the energy per bond ϵ and the hole–hole repulsion V. In the tightly bound regime, the effective perturbative tunnelling of the pair can be described by a second-order process through a virtual, off-resonant state as shown in Fig. 3a. The energy difference is then determined by $\Delta E = E_{\mathrm{init}} - E_{\mathrm{virtual}}$ and depends on the spin background:

$$\begin{aligned}\Delta E_{z\text{-AFM}} &= V + \frac{|J_z|}{4} \quad \Delta E_{z\text{-FM}} = V - \frac{|J_z|}{4} \\ \Delta E_{x\text{-AFM}} &= V - \frac{J_\perp}{4} \quad \Delta E_{x\text{-FM}} = V + \frac{J_\perp}{4}.\end{aligned} \tag{17}$$

The coupling between the initial and virtual states as well as from the virtual to the final states scales with the bare tunnelling t and, further, the perturbative description includes a factor χ associated with the finite overlap between states in the spin sector. In general, the factor $\chi = \chi(T)$ is spin-background-dependent and time-dependent, with the timescale corresponding to the equilibration time of the spin background. At late times, we find the effective perturbative tunnelling $-t^{(\mathrm{pert})} = \chi t^2/\Delta E > 0$.

As well as the perturbative pair tunnelling process, the long-range dipolar tunnellings induce a direct tunnelling of amplitude $-t^{(\mathrm{dir})} = -t/8$, in which one hole traverses the other. In our 1D scheme, the sign of the tunnelling t depends on the angle θ relative to the magic angle $\theta_m = 54.7°$. The resulting total effective pair mass is then given by $t^{(\mathrm{eff})} = t^{(\mathrm{pert})} + t^{(\mathrm{dir})}$, which we investigate by the centre-of-mass spreading of the hole pairs (Figs. 3e and 4b). In particular, in the analysis shown Fig. 4, we post-select on snapshots in the $|P\rangle$ basis with $N_h = 2$ holes and bond length $\ell \le 2$, from which we extract the centre-of-mass spreading of the pair; the qualitative analysis is not dependent on our choice of the size of the pair.

As a consistency check of our perturbative pair model, we perform a numerical analysis of the protocol described in Fig. 3 and compare it with a model with couplings between only NN sites. First, we predict the NN model to not experience interference with a direct tunnelling term, leaving only the bare perturbative tunnelling of the pair (Extended Data Fig. 7a). By contrast, the binding energy is not affected by the absence of the dipolar tails and we expect a difference in the binding strength in both cases (Extended Data Fig. 7b). Our predictions derived from perturbation theory are consistent with the numerical simulations corroborating the influence of dipolar tunnellings present in our experiment.

Numerical simulations

The numerical time-evolution simulations presented in the main text and Methods, except Fig. 5c,d, are based on exact diagonalization methods of the Rydberg Hamiltonian (equation (5)), including interactions up to distance $r_{ij} \leq 3$ (in units of lattice sites). We develop an error model to describe the experimental situation, which we introduce in the following in decreasing order of relevance.

State-preparation errors. Initial state-preparation errors are most detrimental to our quench protocol. In particular, atoms with an initial local target state can be falsely prepared in any of the other two Rydberg states or remain in the (non-interacting) ground state.

To model these errors, we sample from a probability distribution, initialize the (falsely prepared) initial product state and time evolve under the Rydberg Hamiltonian. Depending on the errors and the observables, we sample between 500 and 4,000 initial states and take one snapshot in the $|S\rangle$, $|P\rangle$ and $|S'\rangle$ basis after time T. Atoms that remained in the ground state are recaptured and appear as a signal in the snapshot.

The measurements of the bound-state population $P(\ell)$ shown in Figs. 3d and 4a include differences between correlation functions, which are not captured accurately by our error model. To improve the theoretical model, we have checked that including correlated errors in the initial state allows us to obtain better agreement between the numerical simulation and the experimental data. For consistency, we only present simulations underlying the same initial state error model. In the future, it is crucial to develop an error scheme that captures correlated errors to quantitatively compare higher-order correlation functions.

Detection errors. In the experiment, an atom can be falsely detected, for example, during the deexcitation pulse of the $|\downarrow\rangle$ state, an atom in state $|h\rangle$ can decay. This atom is then recaptured and imaged. In the numerical simulations, we include the detection errors by postprocessing snapshots, that is, we randomly flip the bits in a snapshot according to the scheme shown in Extended Data Fig. 2 and the probabilities in equation (3); this procedure requires knowledge about the actual state.

Rydberg lifetime. We use quantum trajectory methods to include the finite lifetime of Rydberg states[50]. For each atomic state, we assume two decay channels:

1. A Rydberg state decays down to the atomic ground state and appears as a signal in the snapshots. We approximate these decay rates by the value of the radiative rates (at temperature 0 K):

$$\Gamma_{60S} \approx \Gamma_{61S} \approx (260\ \mu\text{s})^{-1}$$
$$\Gamma_{60P} \approx (472\ \mu\text{s})^{-1}. \tag{18}$$

2. A Rydberg state has a blackbody-induced transition to other Rydberg states and is lost from the simulation. The decay rates are given by:

$$\Gamma^{\text{BB}}_{60S} \approx \Gamma^{\text{BB}}_{61S} \approx (157\ \mu\text{s})^{-1}$$
$$\Gamma^{\text{BB}}_{60P} \approx (161\ \mu\text{s})^{-1}. \tag{19}$$

We neglect the possibility of blackbody-induced transitions between the states of the computational basis ($|\uparrow\rangle$, $|h\rangle$ and $|\downarrow\rangle$), the rate of which is small compared with the decay rate to other states in the Rydberg manifold.

Positional disorder. At time $T = 0$, the tweezer light is turned off, which projects the trapped spatial wavefunction onto free space, leading to a dispersive wavepacket. Although we do not include the subsequent motion or spin-motion coupling that are expected to be small at the experimental energy and timescales, we model the initial wavefunction spread by including positional disorder. We assume the spatial probability distribution of each atom to be normally distributed around its target position with a standard deviation of $\sigma_{xy} = 0.1\ \mu\text{m}$ (in-plane) and $\sigma_z = 1.0\ \mu\text{m}$ (perpendicular to the plane). For each numerical trajectory, we sample the initial positions of the atom and time evolve the internal states under the Rydberg Hamiltonian with couplings according to the spatial distribution of the atom.

Numerical simulations: 2D AFM

To simulate the dynamics of the initial 2D AFM product state, we apply matrix-product-state methods. In particular, we time evolve under the Hamiltonian in equation (5) using the built-in two-site time-dependent variation principle algorithm (2DTVP) of the TeNPy package[51,52]. All calculations use a maximum bond dimension $m = 1{,}000$ and we choose the time steps $\Delta T = 0.025 \times \frac{2\pi}{|2t|}$. To account for experimental imperfections, we average the local hole probability (see Fig. 5c,d) over 400 trajectories according to initial product states sampled from the error budget shown in Extended Data Fig. 4b. As an indicator for convergence, we analyse the energy density $e(T) = \langle\psi(T)|\ \hat{H}\ |\psi(T)\rangle/L$ and confirm that the deviation of the energy density to the initial state energy density $e(0)$ remains within $\max_T|e(T) - e(0)| \leq 1 \times 10^{-4} \times |t|$ ($\max_T|e(T) - e(0)| \leq 7 \times 10^{-5} \times |t|$) for simulations with long-range Rydberg tails (only NN interactions).

Data availability

All data are available from the corresponding author on request.

47. Weber, S. et al. Tutorial: Calculation of Rydberg interaction potentials. *J. Phys. B: At. Mol. Opt. Phys.* **50**, 133001 (2017).
48. Marder, M., Papanicolaou, N. & Psaltakis, G. C. Phase separation in a *t-J* model. *Phys. Rev. B* **41**, 6920 (1990).
49. Bobroff, J. et al. Absence of static phase separation in the high T_c cuprate $YBa_2Cu_3O_{6+y}$. *Phys. Rev. Lett.* **89**, 157002 (2002).
50. Daley, A. J. Quantum trajectories and open many-body quantum systems. *Adv. Phys.* **63**, 77–149 (2014).
51. Hauschild, J. et al. Tensor network Python. Code available at https://github.com/tenpy/tenpy/. Documentation available at https://tenpy.readthedocs.io/en/latest/ (2018).
52. Hauschild, J. & Pollmann, F. Efficient numerical simulations with Tensor Networks: Tensor Network Python (TeNPy). *SciPost Phys. Lect. Notes* https://doi.org/10.21468/scipostphyslectnotes.5 (2018).

Acknowledgements We thank J. Mögerle, K. Brechtelsbauer and H.-P. Büchler for insightful discussions about encoding spins using three Rydberg states and J. Mögerle for help on the use of the pairinteraction software package[47]. This work is supported by the Agence Nationale de la Recherche (ANR-22-PETQ-0004 France 2030, project QuBitAF), the European Research Council (Advanced Grant no. 101018511-ATARAXIA) and the Horizon Europe programme HORIZON-CL4-2022-QUANTUM-02-SGA (project 101113690 (PASQuanS2.1). R.M. acknowledges support by the 'Fondation CFM pour la Recherche' through a Jean-Pierre Aguilar PhD scholarship. L.H. is supported by the Simons Collaboration on Ultra-Quantum Matter, which is a grant from the Simons Foundation (651440). L.H. and F.G. were supported by the Deutsche Forschungsgemeinschaft (DFG, German Research Foundation) under Germany's Excellence Strategy - EXC-2111 - 390814868 and have received funding from the European Research Council (ERC) under the European Union's Horizon 2020 research and innovation programme (grant agreement no. 948141) – ERC Starting Grant SimUcQuam. S.H. acknowledges support through the Harvard Quantum Initiative Postdoctoral Fellowship in Quantum Science and Engineering. S.G. acknowledges support by Structures (DFG) under Germany's Excellence Strategy EXC2181/1-390900948). D.B. acknowledges support from MCIN/AEI/10.13039/501100011033 (PID2020-119667GA-I00, CNS2022-135781, EUR2022-134067 and European Union NextGenerationEU PRTR-C17.I1).

Author contributions M.Q., G.E., C.C., G.B. and R.M. carried out the experiments, with the help of B.G., L.K. and D.B. L.H. and M.Q. conducted the numerical simulations. L.H., S.H., S.G. and N.-C.C. devised the Rydberg scheme combining dipolar and van der Waals couplings to realize the *t–J* model. A. Bohrdt, F.G., T.L. and A. Browaeys supervised the work. All authors contributed to the data analysis, progression of the project and on both the experimental and theoretical sides. All authors contributed to the writing of the manuscript. Correspondence and requests for materials should be addressed to Antoine Browaeys or Mu Qiao.

Competing interests A. Browaeys and T.L. are cofounders and shareholders of PASQAL. The other authors declare no competing interests.

Additional information

Correspondence and requests for materials should be addressed to Mu Qiao or Antoine Browaeys.

Peer review information *Nature* thanks Xiong-Jun Liu, Ivan Morera Navarro and the other, anonymous, reviewer(s) for their contribution to the peer review of this work.

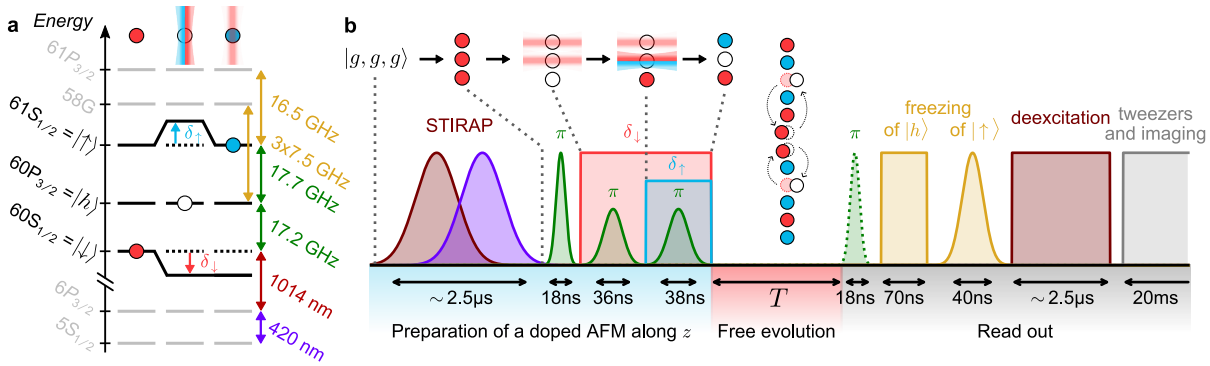

Extended Data Fig. 1 | Protocol for the preparation of a doped antiferromagnet along *z*. a, Involved energy levels and transitions. The states used in the mapping to the *t*–*J*–*V* Hamiltonian are indicated in black. Each of the three columns represents one class of atoms: non-addressed atoms (left column) are prepared in $|\downarrow\rangle$, atoms with both $\delta_\downarrow$ and $\delta_\uparrow$ light shifts (centre column) are prepared in $|h\rangle$ and atoms with only the $\delta_\uparrow$ light shift (right column) are prepared in $|\uparrow\rangle$. **b**, Experimental sequence. After Rydberg excitation using STIRAP, we apply a sequence of microwave pulses combined with the site-resolved light shifts $\delta_\uparrow$ and $\delta_\downarrow$. Then, the light shifts are switched off for duration *T*, during which the system evolves under the *t*–*J*–*V* interactions. To read out the atomic states, we first perform two 'freezing' pulses to stop the dynamics, which respectively act on states $|h\rangle$ and $|\uparrow\rangle$. Then, we deexcite the atoms from $|\downarrow\rangle$ to the ground-state manifold, switch on the tweezers and image the recaptured atoms using fluorescence. An extra microwave π-pulse (dotted green line) can be used to read out the state $|h\rangle$.

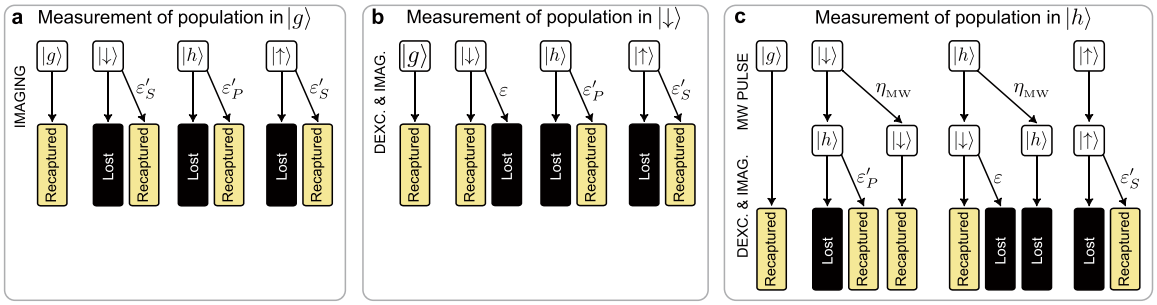

Extended Data Fig. 2 | Simplified error tree associated to our detection schemes. The three panels **a**, **b** and **c** show the detection errors for the populations in, respectively, $|g\rangle$, $|\downarrow\rangle$ and $|h\rangle$. For each scheme, we represent the probability of detection events for the four states $|g\rangle$, $|\downarrow\rangle$, $|h\rangle$ and $|\uparrow\rangle$, at the first order in the detection errors ε, $\varepsilon'_{S,P}$ and η_{MW}.

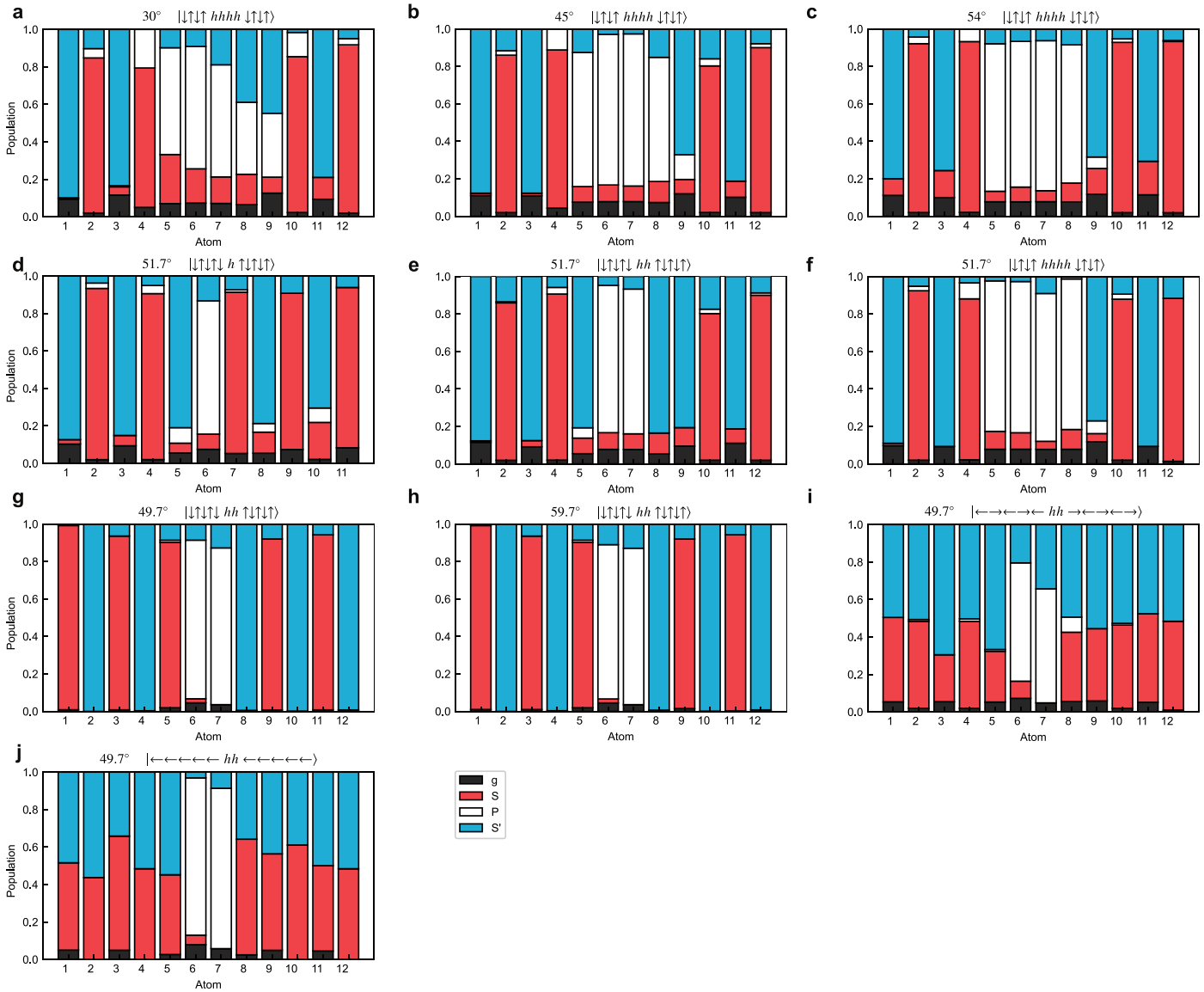

Extended Data Fig. 3 | State-preparation errors for 1D chain. Site-resolved population measurements for different initial state preparations at various angles θ relative to the quantization axis, showing the initial state-preparation error. The detection error is corrected through the maximal likelihood method, using the cost function of equation (4). **a**–**c**, Population distributions for an initial Néel state with four holes in the centre at $\theta = 30°$ (**a**), $\theta = 45°$ (**b**) and $\theta = 54°$ (**c**). **d**–**f**, population distributions for different numbers of holes at $\theta = 51.7°$: one hole (**d**), two holes (**e**) and four holes (**f**). **g**–**j** Population distributions for different magnetic backgrounds: AFM along z at $\theta = 49.7°$ (**g**) and $\theta = 59.7°$ (**h**) and AFM and FM along x (**i**,**j**). The measured populations are shown for the four possible states: ground state (black), $|\downarrow\rangle$ (red), $|h\rangle$ (white) and $|\uparrow\rangle$ (blue). These errors are systematically included in all of the numerical simulations presented in the main text.

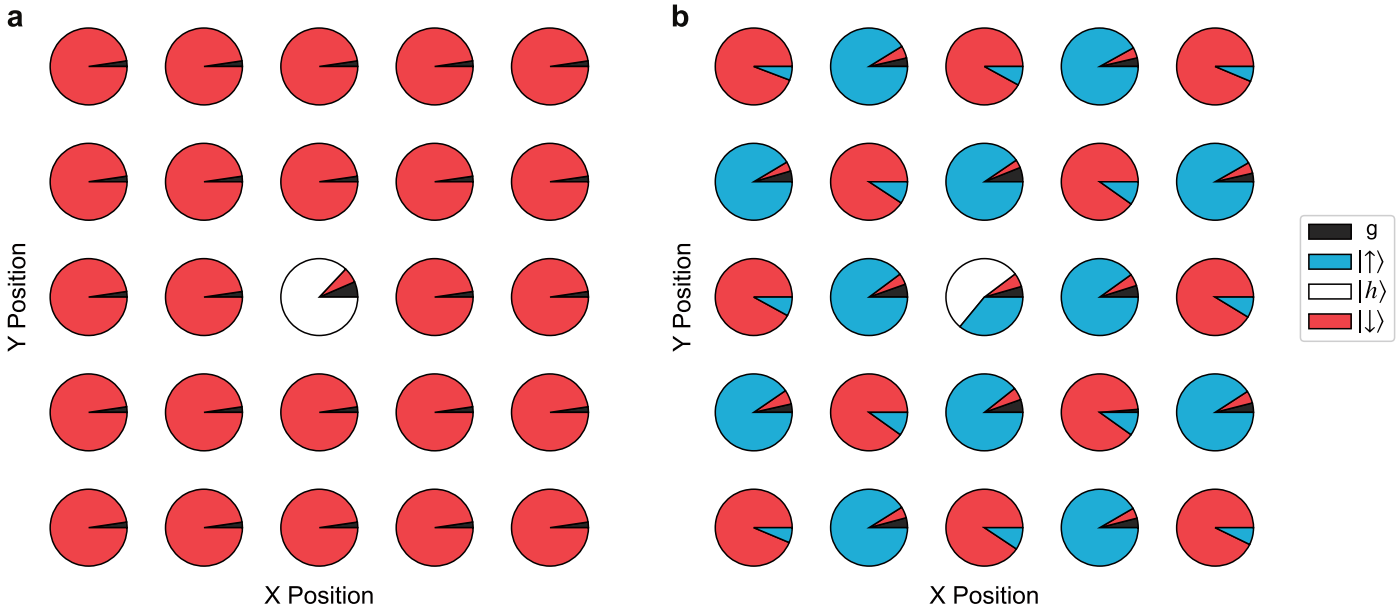

Extended Data Fig. 4 | State-preparation errors for 2D array. a, Population measurement for a FM state (red) with a single hole $|h\rangle$ (white) at the centre. **b**, Population measurement for a Néel-ordered state alternating between $|\uparrow\rangle$ (blue) and $|\downarrow\rangle$ (red) with a central hole. The pie charts at each site show the relative populations of the four possible states: ground state (black), $|\downarrow\rangle$ (red), $|h\rangle$ (white) and $|\uparrow\rangle$ (blue). Detection errors have been corrected using a maximum likelihood estimation method. The observed state-preparation fidelities are incorporated into the numerical simulations presented in the main text.

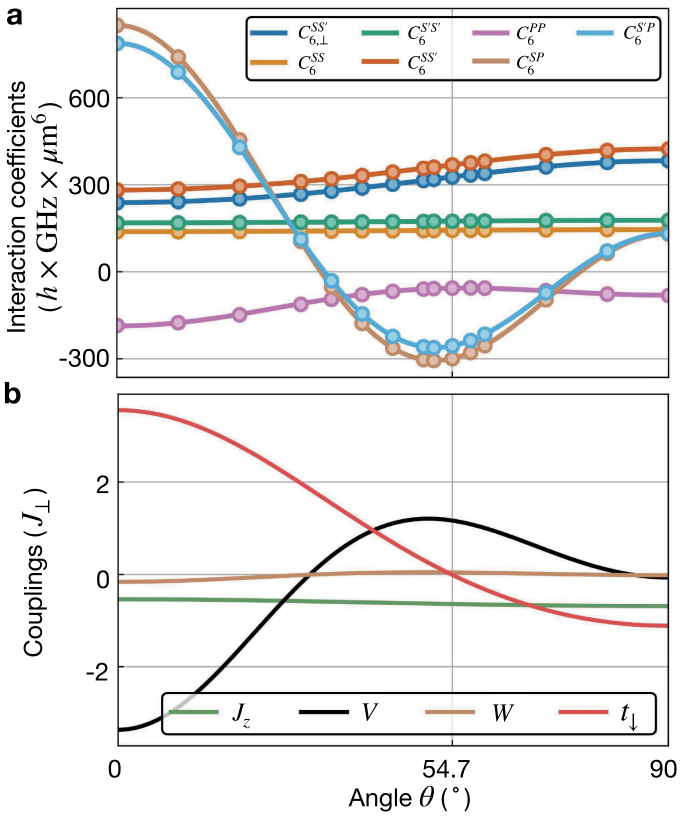

Extended Data Fig. 5 | Angular dependence of interactions. a, The van der Waals interaction coefficients $C_6^{\alpha\beta}(\theta_{ij})$ are calculated from the Rydberg pair interactions at a magnetic field magnitude of $B = 50$ G for various angles θ_{ij} between the inter-atomic axis and the magnetic field (solid markers). We fit the each coefficient to the function $f^{\alpha\beta}(\theta_{ij}) = F_1^{\alpha\beta} + F_2^{\alpha\beta}\cos^2\theta_{ij} + F_3^{\alpha\beta}\cos^4\theta_{ij}$ (solid line). **b**, The coupling amplitudes of the t–J–V–W model are computed using Extended Data Table 1. The spin–hole interaction $W/J_\perp \approx 0$ for all angles and hence we can neglect it for all practical purposes in our interpretation of the experimental results. Note that numerical calculations are based on the full Rydberg Hamiltonian.

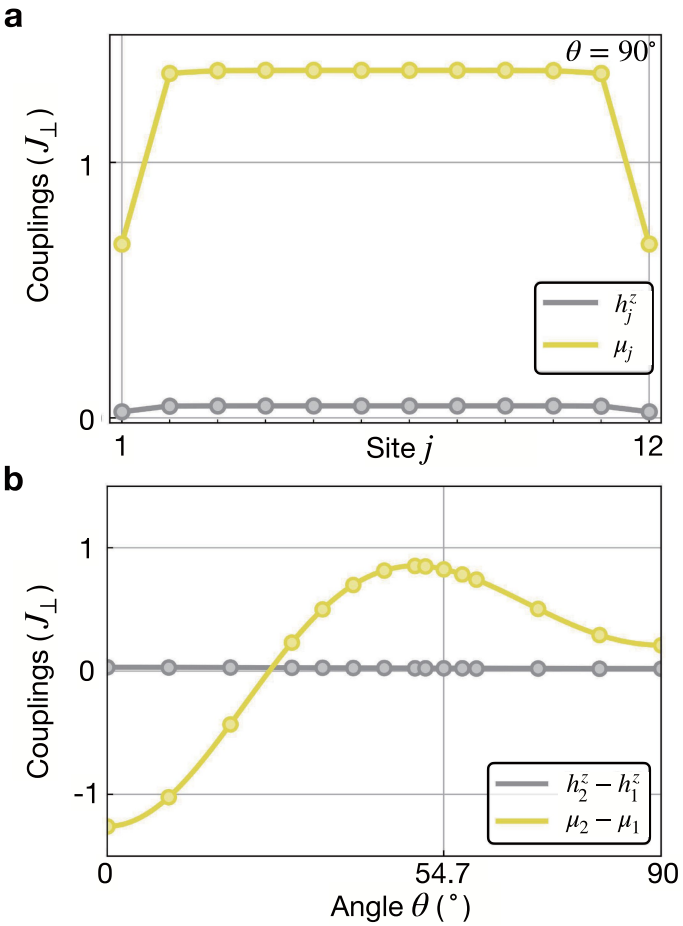

Extended Data Fig. 6 | Boundary terms. Site-dependent field terms h_j^z and μ_j calculated as in Fig. 5. **a**, Fields at angle $\theta = 90°$ for the 12-site chain realized in the experiment. As the difference in magnitude between the fields at the boundary compared with the bulk is large, those terms can play a role in the presence of boundaries. **b**, To quantify the boundary terms, we plot the difference of the fields between sites 2 and 1 as a function of the angle θ.

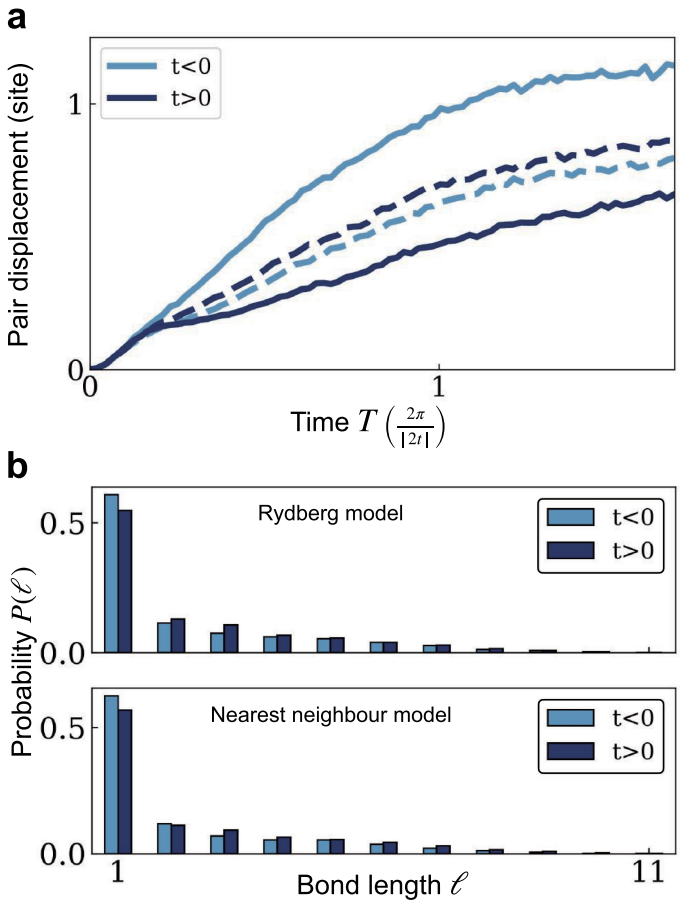

Extended Data Fig. 7 | Interference from NNN tunnellings t'. We numerically study the time evolution of an initial hole pair in the $L = 12$ z-AFM without errors under: (1) the full Rydberg Hamiltonian and (2) a model with interactions truncated beyond the NN couplings. The angles are chosen to be $\theta = 49.7°$ ($t < 0$) and $\theta = 59.7°$ ($t > 0$) (see Fig. 3). **a**, We plot the centre-of-mass pair displacement of the pair. The solid line corresponds to model (1) and corresponds to an ideal experiment without errors; the difference in the centre-of-mass pair displacement is clearly visible, which we explain by the interference between perturbative and NNN tunnelling t'. When we consider the model with only NN couplings (2), shown as dashed lines, the strong difference in the pair displacement disappears. **b**, We compare the pair distance histograms at time $T = 1.6 \times \frac{2\pi}{|2t|}$ and find that the hole is more tightly bound for $\theta = 49.7°$ than for $\theta = 59.7°$, independent of the range of tunnellings. This is consistent with our perturbative description of the pair, for which the binding energy only depends on the hole–hole repulsion V and spin interaction J_z.

Extended Data Table 1 | Mapping of interaction strengths

t-J-V	Rydberg
$t_\downarrow(\theta_{ij})$	$-C_3^{SP}(1-3\cos^2\theta_{ij})$
$t_\uparrow(\theta_{ij})$	$-C_3^{S'P}(1-3\cos^2\theta_{ij})$
$J_\perp(\theta_{ij})$	$2\cdot C_{6,\perp}^{SS'}(\theta_{ij})$
$J_z(\theta_{ij})$	$C_6^{SS}(\theta_{ij})+C_6^{S'S'}(\theta_{ij})-2C_6^{SS'}(\theta_{ij})$
$V(\theta_{ij})$	$\frac{1}{4}\left[C_6^{SS}(\theta_{ij})+C_6^{S'S'}(\theta_{ij})+2C_6^{SS'}(\theta_{ij})\right]-C_6^{SP}(\theta_{ij})-C_6^{S'P}(\theta_{ij})+C_6^{PP}(\theta_{ij})$
$W(\theta_{ij})$	$C_6^{S'P}(\theta_{ij})-C_6^{SP}(\theta_{ij})+\frac{1}{2}\left[C_6^{SS}(\theta_{ij})-C_6^{S'S'}(\theta_{ij})\right]$
$h_j^z(\theta_{ij})$	$\frac{1}{2}\sum_i\frac{1}{r_{ij}^6}\left[C_6^{S'S'}(\theta_{ij})-C_6^{SS}(\theta_{ij})\right]$
$\mu_j(\theta_{ij})$	$\frac{1}{4}\sum_i\frac{1}{r_{ij}^6}\left[C_6^{SS}(\theta_{ij})+C_6^{S'S'}(\theta_{ij})+2C_6^{SS'}(\theta_{ij})-2C_6^{SP}(\theta_{ij})-2C_6^{S'P}(\theta_{ij})\right]$

The coupling strength of the *t–J–V* model (equations (1) and (5)) are related to the atomic pair interactions.

Extended Data Table 2 | Interaction strengths of the bosonic *t–J–V* model

θ (°)	a (μm)	$t_\downarrow$ (MHz)	$t_\uparrow$ (MHz)	$J_\perp$ (MHz)	J_z (MHz)	V (MHz)	W (MHz)	h^z (MHz)	μ (MHz)
30	9.9	-1.10	-1.05	0.57	-0.33	-0.10	-0.01	0.02	0.14
45		-0.43	-0.41	0.64	-0.40	0.72	0.03	0.02	0.53
49.7		-0.22	-0.21	0.67	-0.42	0.81	0.03	0.02	0.58
51.7		-0.13	-0.13	0.68	-0.43	0.82	0.03	0.02	0.58
54.7		0.03	0.02	0.70	-0.45	0.82	0.03	0.02	0.58
59.7		0.21	0.20	0.72	-0.47	0.74	0.02	0.02	0.54
90	12	0.51	0.48	0.26	-0.18	-0.02	-0.00	0.01	0.05

Calculated values of the interaction strength for the experimental configurations used in the main text; the full angle dependence can be found in Fig. 5b. The calculated values indicate that W and h_z are typically negligible compared with other energy scales. Although the chemical potential μ can be important, its uniformity in the bulk of a regular lattice means that its primary physical influence is expected at the system boundaries.